

# Defective black Ti<sup>3+</sup> self-doped TiO<sub>2</sub> and reduced graphene oxide composite nanoparticles for boosting visible-light driven photocatalytic and photoelectrochemical activity

*Shanchi Wang,<sup>a</sup> Jingsheng Cai,<sup>a</sup> Jiajun Mao,<sup>a</sup> Shuhui Li,<sup>ab</sup> Jiali Shen,<sup>a</sup> Shouwei Gao,<sup>a</sup> Jianying Huang,<sup>a</sup> Xiaoqin Wang,<sup>a</sup> Ivan P. Parkin,<sup>b</sup> Yuekun Lai,<sup>\*a</sup>*

a. National Engineering Laboratory for Modern Silk, College of Textile and Clothing Engineering, Soochow University, Suzhou 215123, P. R. China.

b. Materials Chemistry Research Centre, Department of Chemistry, University College London, London, UK

\*Correspondence to: Yuekun Lai (E-mail: [yklai@suda.edu.cn](mailto:yklai@suda.edu.cn))

**Abstract:** We present a facile and environmentally friendly way to successfully build partially reduced titanium dioxide nanoparticles integrated with reduced graphene oxide composite nanosheets (RGO/TiO<sub>2-x</sub>) through an environmental solvothermal method at relatively low temperature. The Ti<sup>3+</sup> self-doping of TiO<sub>2-x</sub> is conducive to enhance its visible light absorption, and the existence of RGO as the electron receiver makes the electrons on TiO<sub>2-x</sub> transport better to its surface, effectively promoting the separation of electrons and holes. Experiments on photocatalytic degradation of methylene blue dye and phenol colorless organic pollutant by visible light demonstrate that the RGO/TiO<sub>2-x</sub> assemblies exhibit the highest photocatalytic activity, and that methylene blue solution concentration of used in the experiment is 40 mg L<sup>-1</sup>, which was more higher than the concentration (10 mg L<sup>-1</sup>) used in many of reported articles. Compared to the pure TiO<sub>2</sub> and TiO<sub>2-x</sub>, the photodegradation efficiency of methylene blue and phenol can be increased to 100% within 120 min and 150 min under visible

light. Moreover, the mineralization rates of MB, such as the total organic carbon (TOC) degradation rate, can reach to 75.7%, 86.6 % and 89.4% for m-RGO/TiO<sub>2-x</sub>, respectively. And the reaction efficiency of RGO/TiO<sub>2-x</sub> is basically not much changed after 4th cycles, suggesting its excellent photocatalytic stability.

**Keywords:** Ti<sup>3+</sup> self-doping, TiO<sub>2</sub> nanoparticle, reduced graphene oxide, visible-light photocatalyst, photoelectrochemical activity

## 1. Introduction

Harvesting solar energy efficiently is important to achieving a sustainable energy supply and reduce environmental impact.[1] Artificial photosynthesis has been widely explored, which will convert directly solar energy into chemical energy. Over the past few years, the photocatalysis of semiconductor has obtained widespread concerns as potential solutions to help solve the problem of the worldwide environmental impact and energy shortage.[2-4] Among a variety of photocatalytic semiconductor materials, titanium dioxide is the most frequently used photocatalyst owing to its unique chemical stability, low cost, excellent recyclability, and nontoxicity.[5,6] Nevertheless, the large band gap extent (3.2 eV for anatase) of TiO<sub>2</sub> seriously restrains its optical absorption to only UV radiation, which makes up only 3–5% of the solar spectrum at sea-level. Furthermore, the fast recombination efficiency of photogenerated electrons with holes and the loss of carrier during electron transport also greatly weakens its photocurrent conversion efficiency. These drawbacks hinder the performance and application of TiO<sub>2</sub> as an efficient photoelectrocatalytic material.[7-9] Therefore, many researchers have attempted to expand the range of TiO<sub>2</sub> optical response from ultraviolet to visible region in order to better capture solar power, and to reduce the recombination efficiency of photogenerated electrons with holes.[10,11]

During the past few decades, to make the absorbance of TiO<sub>2</sub> susceptible to visible light, many projects have been devoted to introduce intermediate gap states into the whole band gap of TiO<sub>2</sub> by incorporating dopants process at the O and/or Ti sites.[5,12,13] Of the existing doping methods, self-doping could provide a more efficient alternative compared with metal or nonmetal doping which can lead to thermolability and increase carrier recombination and trapping centers.[14-18] Reduced defective TiO<sub>2</sub> (TiO<sub>2-x</sub>) containing Ti<sup>3+</sup> self-doping has shown the good visible light absorption and has attracted an attractive interest in recent years.[19-21] It was reported that black TiO<sub>2</sub> first produced in 2011 via hydrogenation is an effective approach by Chen et al. in narrowing the light absorption band gap of TiO<sub>2</sub> into about 1.5 eV with optical initiation about 1.0 eV.[22] After the discovery of black TiO<sub>2</sub> nanomaterials, the application of carbon black nanostructures in the field of energy has been a hot spot and various methods for synthesizing black TiO<sub>2</sub> have been reported, which show a great breakthrough in the field of photocatalytic performance.[22-26] However, most reported methods of preparing black TiO<sub>2</sub>, including hydrogen thermal treatment or chemical reduction of the TiO<sub>2</sub> at high temperature, have multiple steps, uneconomical facilities and/or harsh synthesis conditions that make them difficult to realize for practical use.[27] Therefore, there is still a serious challenge to develop an economical and simple method for the synthesis of reduced TiO<sub>2</sub> with good stability and dispersion under mild conditions for practical use.

To overcome the problem of the fast photoinduced electron–hole pairs recombination rate of TiO<sub>2</sub>, some reports were committed to decorating TiO<sub>2</sub> with some electronic acceptors, such as carbon-based materials or noble metal nanoparticles.[28-33] However, the cost of noble metal nanoparticles is high, and it is not suitable for large-scale operation. Therefore, carbon-based materials and low cost additives, may

be an effective substitute for rare noble metals. Previous reports showed that TiO<sub>2</sub>-carbon hybrid materials, consisting of carbon nanotubes, activated carbon, graphene and carbon fullerenes, could show better photocatalytic properties than absolute TiO<sub>2</sub>. [34-36] Recently, graphene (GR) has been used as an ideal carrier for loading with TiO<sub>2</sub> nanoparticles, due to the exceptional electrical, thermal, and mechanical properties with high electron mobility, thermal conductivity, and Young's modulus, which can effectively boost the transport of electrons and the separation of electrons and holes. [37,38] Furthermore, various methods, such as hydrothermal, physical compounding, electro-deposition and self-assembly techniques have been used for the fabrications of TiO<sub>2</sub>-graphene composites. [39-41] For example, Williams et al. proposed that a physical complex of photoactive TiO<sub>2</sub>-graphene composites was synthesized through a ultra-violet assisted reduction technique. [42] Ge et al. demonstrated that a combination of simple electrolytic deposition and carbonation process to deposit RGO films on highly ordered TiO<sub>2</sub> NATs, which were formed using a two-step electrochemical anodization technique with an appropriate volume ratio of H<sub>2</sub>O and NH<sub>4</sub>F, which showed 2.9 times improved photodegradation efficiency than pure TiO<sub>2</sub>. [42] However, there are unavoidable disadvantages of these traditional strategies, such as the addition of toxic reductant, the requirements of high pressure or temperature, acid or alkali additives, long time and high energy consumption. Consequently, it is extremely important to develop a clean technology for the reduction of GO, which becomes a key step in the research of graphene-semiconductor composites.

Herein, we discussed a simple method to construct partially reduced TiO<sub>2</sub> nanoparticles integrated with reduced graphene oxide (RGO/TiO<sub>2-x</sub>) nanosheets, using a relatively environmentally-friendly one-step hydrothermal technique at

comparatively low temperature (220 °C) (Scheme 1). The as-prepared compound materials could efficiently conquer the above-mentioned shortcomings to a certain extent. First of all, the existence of  $\text{Ti}^{3+}$  states would not only change  $\text{TiO}_2$  electron structure, such as narrowing the bandgap through introduction of mid-gap states, but also extend the range of light absorption into visible light region. Perhaps the combination with reduced graphene oxide will also increase the visible light absorption range, which could enhance the photocatalytic effect. In addition, due to the addition of reduced graphene oxide nanosheets as an electron acceptor, the photoinduced electrons could be successfully transferred to the RGO nanosheet layer from the conduction band edge of  $\text{TiO}_{2-x}$  nanoparticles, which would effectively promote the interfacial transport of photogenerated electrons and the separation of charges. Furthermore, with this method, the  $\text{Ti}^{3+}$  self-doping and the reduction of GO would be obtained, simultaneously, with no toxic reductants needed to be used during the compound reaction. To detect the photocatalytic performance of the as-prepared photocatalysts, the photoelectrochemical properties and photodegradation efficiency of the new composition were investigated and characterized. It was found that RGO/ $\text{TiO}_{2-x}$  composites showed excellent photocatalytic performance due to low recombination rate of photogenerated carriers and high visible optical absorption capacity.

## **2. Experimental Section**

### *2.1. Preparation of GO Sheets*

Graphene oxide (GO) was synthesized by a modified Hummers method using natural graphite powder. In brief, under ice bath conditions, natural graphite powder (2 g) was dissolved in 46 mL of concentrated sulfuric acid, then 6.0 g  $\text{KMnO}_4$  was slowly added to the above mixture under stirring. After that, the mixture was maintained at

35 °C for 2 hours, carefully adding 100 mL deionized water when the temperature was gone up to 80 °C. The temperature continues to rise to 95 °C for 10 minutes and then poured into 300 mL deionized water. Eventually, the final solution was washed by centrifugation several times with diluted HCl solution, deionized water and ethylalcohol. The graphene oxide powder was obtained by freeze-drying.

## *2.2. Fabrication of Partial Reduced TiO<sub>2</sub> Nanoparticles Integrated with Reduced Graphene Oxide Nanosheets*

A certain amount of the synthesized graphene oxide powder was dissolved in a mixed solution containing 20 mL absolute ethyl alcohol and 0.1 mL deionized water under fierce magnetic stirring for 1 h, forming a stable brown graphene oxide suspension. Then, tetrabutyl titanate (TBOT, C.P.) with 0.5 mL were added into 20 mL absolute ethanol in the process of stirring, and subsequently the mixture was stirred by ultrasonic processing for 1 h. After that, under stirring conditions, the mixture consisted of 0.5 mL TBOT and 20 mL absolute ethanol was dropwise added to the above brown suspension. Subsequently, the obtained compound suspension was transferred to a 50 mL Teflon-lined autoclave. The autoclave was maintained at 220 °C for 10 h, and then natural coming to room temperature. The prepared sample was washed by centrifugation with deionized water and absolute ethanol 3 times and dried in an oven at a temperature of 60 °C overnight for further use and performance characterization. The resulting sample was noted as m-RGO/TiO<sub>2-x</sub> where m is defined as the added amount of GO (m = 0.1, 0.2, 0.3 g). For comparison, partially reduced TiO<sub>2</sub> (TiO<sub>2-x</sub>) was obtained on the basis of the previous report.[43]

## *2.3. Characterization*

The morphology and surface structure of RGO/TiO<sub>2-x</sub> were observed by field emission scanning electron microscopy (FE-SEM, Hitachi S-4800) at 3.0 kV. The

internal and surface microstructure of the RGO/TiO<sub>2-x</sub> product was explored by a transmission electron microscope (TEM, FEI Tecnai G20) at 200 kV and a high-resolution transmission electron microscope (HRTEM, F20). An energy dispersive X-ray spectrometer (EDS) fitted to SEM and TEM was applied for elemental analysis. The X-ray photoelectron spectroscopy tests (XPS) (Kratos Axis-Ultra HAS) were utilized to analyze chemical constitution and element states using an Al-K $\alpha$  X-ray ( $h\nu = 1486.6$  eV) radiation source at 100 W. The X-ray diffraction (XRD) measurement (Philips, X'pert-Pro MRD, Japan) of the samples were presented to identify the crystal phases by an X-ray diffractometer with intense Cu K $\alpha$  radiation. Raman spectra were analyzed to identify the substance and analyze the nature of the substance by A HORIBA JOBIN YVON (HR800) spectctrometer. Fourier transform infrared (FTIR) spectra were measured with a 4000–400 cm<sup>-1</sup> scanning range on a Varian Scimitar 1000 spectrophotometer. UV-vis diffuse reflection spectroscopy (UV-DRS) was obtained on compressed disk samples in the range of 800–200 nm by a UV-3600 spectrophotometer at room temperature. Photoluminescence (PL) measurements of the samples were obtained using fluorescence spectroscopy (HOKIBA JOBIN YVON, FM4P-TCSPC) with Xenon lamp as an excitation light source ( $\lambda = 362$  nm).

#### *2.4. Photoelectrochemical measurements*

The indispensable photoelectrochemical measurements of all as-prepared samples were performed in a quartz beaker via chronoamperometry, electrochemical impedance spectroscopy and the linear sweep voltammetry curves in a standard three electrodes system with a 0.1 M Na<sub>2</sub>SO<sub>4</sub> aqueous electrolyte solution using a PGSTAT302N electrochemical workstation (AUTOLAB, Switzerland). Working electrode was obtained as follows: as-prepared sample (5 mg) was dissolved in 500  $\mu$ L isopropanol and 50  $\mu$ L Nafion (0.5%) stirring ultrasonically for one hour, and then 3.0  $\mu$ L of the

above-mentioned suspension was dip-coated onto glassy carbon electrode (3 mm in diameter). Platinum wire and saturated calomel electrode would serve as the counter electrode and the reference electrode, respectively. To characterize the interfacial properties of the electrodes, photocurrent measurements were carried out by measuring the photocurrent densities with bias potential of 0.2 V vs SCE. The EIS measurements were defined at a 5 mV AC voltage amplitude with a frequency range of  $10^5$ – $10^{-1}$  Hz. Linear sweep voltammetry curves were tested at  $10 \text{ mV}\cdot\text{s}^{-1}$  scanning rate, and swept linearly the voltage range between -0.5 V and 1.0 V vs SCE. The working electrodes were irradiated by a 500 W Xenon arc lamp with a distance of 20 cm between the beaker and the light source.

### 2.5. Photocatalytic measurements

Photocatalytic properties of all samples were characterized by the degradation for MB dye contaminant with a superior initial concentration of  $40 \text{ mg L}^{-1}$  (pH = 8.5) or  $10 \text{ mg L}^{-1}$  phenol colorless organic pollutant under visible irradiation by using a PS-GHX photochemical reactor. A 500 W Xe arc lamp with a Ultraviolet cutoff filter (420 nm) was used as the simulated visible-light source. The corresponding distance between the light source and the quartz tube was 60 mm. Before each light irradiation, 50 mg of Photocatalytic sample was added into 50 mL of MB or phenol aqueous solution. The MB and phenol aqueous solutions with samples were ultrasonicated for 10 min and later stirred 12 h or 1 h in the darkroom to ensure complete an adsorption–desorption equilibrium. At certain time intervals, a certain amount of suspensions was taken out and immediately centrifuged for subsequent UV-vis measurement (Hitachi, UV-1080, Japan) of the supernatant to calculate the concentration of MB and phenol contaminant at the wavelength of 463 nm or 270 nm. The mineralization rates of MB were obtained using the total organic carbon (TOC) equipment (Multi N/C 2100, TOC/TN). To

determine the stability of the prepared photocatalysts, the used photocatalysts were recycled and the composites were recovered after a photocatalytic experiment, washing with ethylalcohol and deionized water three times and drying with 60°C overnight. In order to detect the effect of the active groups in the photocatalytic process, a variety of scavengers, consisting of 1,4-benzoquinone reagent (BQ, as a superoxide ( $O_2^{\bullet-}$ ) radical scavenger), ethylenediaminetetraacetic acid disodium salt (EDTA-2Na) as a hole ( $h^+$ ) scavenger and isopropanol (IPA, as a hydroxyl ( $\bullet OH$ ) radical scavenger), were introduced into the MB aqueous solution. Detailed schematic diagram for nanomaterials synthesis and photoelectrochemical/photocatalytic performance research is exhibited in Scheme 1.

### 3. Results and Discussion

As shown in Fig. 1a and b, field emission scanning electron microscopy (FESEM) and transmission electron microscopy (TEM) images of the RGO/TiO<sub>2-x</sub> composites show the typical morphology and internal structure of the products. A FESEM image (Fig. 1a) clearly revealed complete and uniform coating of TiO<sub>2</sub> onto the RGO sheets. TEM image (Fig. 1b) further revealed the nature of the ultrathin sheet and the fact that TiO<sub>2</sub> nanoparticles with the size of ~8 nm are homogeneously packed on the sheet, which perfectly fitted the images from FESEM. Fig. 1c shows the energy dispersive X-ray spectrometer (EDS) spectrum of a wide area of the RGO/TiO<sub>2-x</sub> composite and demonstrated that the sample is made up of C, O, Ti elements, and the corresponding atomic ratios are 63.2 %, 25.7 % and 11.1 %, respectively. In addition, the corresponding element mapping (Fig. 1d) images of the C, O and Ti elements demonstrated a highly homogeneous distribution on the surface of the sheets. These results deduced that TiO<sub>2</sub> nanoparticles were efficiently dispersed on the RGO sheets.

High-resolution TEM data (HRTEM) (Fig. 2a) indicated a wide variety of TiO<sub>2</sub> nanoparticles are supported on the RGO sheets. They have a defined crystal structure with a lattice distance (0.35 nm) equivalent to the crystal structure of anatase (101) plane. The corresponding selected-area electron diffraction (SAED) (Fig. 2b) of RGO/TiO<sub>2-x</sub> composite further confirmed its polycrystalline nature. Fig. 2c is the narrow range EDX element mapping which was further utilized to prove the existence and distribution of major elements, which is also consistent with the EDS spectrogram of FESEM.

To investigate the successful doping of Ti<sup>3+</sup> or oxygen vacancies, the chemical state and effective integration of RGO and TiO<sub>2</sub> were demonstrated by X-ray photoelectron spectroscopy (XPS). The spectrum (Fig. 3a) proved the existence of C, O, and Ti with the binding energy peaks for C 1s (284.8 eV), O 1s (531.0 eV) and Ti 2p (465.3 eV), respectively.

The XPS spectra of high resolution for C 1s, O 1s and Ti 2p regions of the RGO/TiO<sub>2-x</sub> are indicated in Fig. 3b-d. The measured spectra were conveniently separated into the desired component peaks after subtracting the spectral background by the Shirley method. Firstly, as displayed in Fig. 3b, the Ti 2p XPS signal of the RGO/TiO<sub>2-x</sub> compound unveiled peaks at 465.6 and 459.8 eV in the Ti<sup>4+</sup> state corresponding to Ti 2p<sub>1/2</sub> and Ti 2p<sub>3/2</sub> splitting photoelectrons of spin-orbital coupling, and the peaks, which located at 464.8 eV and 459.4 eV, were respectively corresponding to the binding energy of Ti<sup>3+</sup> 2p<sub>1/2</sub> and Ti<sup>3+</sup> 2p<sub>3/2</sub>.<sup>[44,57]</sup> The detailed contents of Ti<sup>3+</sup> in the composites were made by two distinct fitting peaks, consisting of Ti<sup>4+</sup> and Ti<sup>3+</sup>, and the peak area ratio of Ti<sup>4+</sup>: Ti<sup>3+</sup> is about 2.8: 1, indicating that the Ti<sup>3+</sup> is around 35% within the composite material. Compared to pure TiO<sub>2</sub>, the peak that appeared at 459.7 eV as shown in Fig. S1a was shifted to the higher energy regions,

which was due to the electron density from  $\text{TiO}_2$  to RGO in the  $\text{RGO/TiO}_{2-x}$  composite.[45,46]

O 1s XPS narrow spectrum (Fig. 3c) of the  $\text{RGO/TiO}_{2-x}$  compound exhibited peaks at 530.9 eV and 532.6 eV respectively corresponding to the lattice oxygen (Ti–O) in  $\text{TiO}_2$ , and to C–OH and/or C–O=C species due to the present of RGO.[47] The peak value at 531.4 eV was attributed to O–Ti<sup>3+</sup>,[46] which is in accordance with the corresponding Ti 2p XPS data. In comparison with absolute  $\text{TiO}_2$ , the O 1s of the  $\text{RGO/TiO}_{2-x}$  compound occurred a certain degree of binding energy migration toward higher energy, which may be on account of the extra electrons (bending effect) of the oxygen defects in crystal lattice structure of the  $\text{TiO}_2$  (Fig. S1b).[5] C 1s XPS spectrum (Fig. 3d) revealed the main peak located at 284.7 eV binding energy, which corresponded to the C–C coordination. The peak at 285.9 eV was classified as the oxygen bound species C–O. It was clear that there was no C=O peak, indicating the efficient reduction of the oxygen-containing functional group in GO during the hydrothermal process.[48] The above results show that the hydrothermal reaction simultaneously carries Ti<sup>3+</sup> doping and graphene reduction.

X-ray diffraction (XRD) spectra (Fig. 4) were performed to further detect the crystalline phases of  $\text{TiO}_2$ ,  $\text{TiO}_{2-x}$ , m-RGO/ $\text{TiO}_{2-x}$  and the physical mixture of 0.2g RGO and  $\text{TiO}_{2-x}$  (0.2-RGO+ $\text{TiO}_{2-x}$ , Fig. S3). In the XRD full spectrum (Fig. 4a), the diffraction peak of  $\text{TiO}_2$  at 25.3°, 37.8°, 47.9°, 54.0°, 54.9°, 62.5° and 70.3° corresponded to the (101), (004), (200), (105), (211), (204) and (220) crystal faces of anatase  $\text{TiO}_2$  planes, respectively.[47,59] It could be seen that there are similar peaks for  $\text{TiO}_2$ ,  $\text{TiO}_{2-x}$ , m-RGO/ $\text{TiO}_{2-x}$  and 0.2-RGO+ $\text{TiO}_{2-x}$ . Nevertheless, as can be seen from Fig. 4b which is an enlarged view of the (101) plane in Fig. 4a, it was noteworthy that the (101) characteristic peak of these samples of  $\text{TiO}_{2-x}$ , m-RGO/ $\text{TiO}_{2-x}$  and 0.2-

RGO+TiO<sub>2-x</sub> were clearly shifted towards lower 2θ values in comparison with pristine TiO<sub>2</sub>. This change of crystal structure could be due to the existence of Ti<sup>3+</sup> or oxygen vacancies through hydrothermal reaction.[49] Compared with Fig. S2 which showed the XRD pattern of graphene oxide, we can see that there is no characteristic diffraction peak of graphite oxide. This could be due to the disruption of the ordered layered structure of graphite oxide by ultrasonic dispersion and subsequent hydrothermal treatment, resulting in the formation of partially reduced graphene oxide, coupled with the TiO<sub>2</sub> nanoparticles were formed on the surface of the graphene oxide layer, which hindered the orderly deposition of the graphene oxide layer.[47] The XRD measurements analyses show that Ti<sup>3+</sup> doping and graphene oxide reduction occurred simultaneously and were carried out through the hydrothermal process, which is consistent with the XPS.

Raman spectra were measured to explore the crystal structure and surface compositions of RGO and TiO<sub>2</sub> in the composite structures (Fig. 5a) of GO, TiO<sub>2</sub>, TiO<sub>2-x</sub> and m-RGO/TiO<sub>2-x</sub>. The pure TiO<sub>2</sub> displayed four obvious bands located at 142.5, 392.9, 511.3, and 636.4 cm<sup>-1</sup>, which were consistent with the specifically characteristic peaks of anatase TiO<sub>2</sub> phase and confirmed by the XRD analysis.[46] The Raman peaks of m-RGO/TiO<sub>2-x</sub> showed all peaks of the anatase TiO<sub>2</sub> and graphene, which further demonstrated the successful integration of TiO<sub>2</sub> on graphene. However, Fig. 5b shows the enlarged view of the peak (142.5 cm<sup>-1</sup>) of the Raman spectra, which showed an obvious red-shift compared with pristine TiO<sub>2</sub>. [50] The G band is a distinctive characteristic of the sp<sup>2</sup> hybrid carbon materials. However, the D band is attributable to the sp<sup>3</sup> defects inside the hexagonal graphitic framework.[48] In the enlarged Raman spectrum (Fig. 5c) of the D band (1326 cm<sup>-1</sup>) and G band (1582 cm<sup>-1</sup>) of GO and m-RGO/TiO<sub>2-x</sub>, there was an increase in the D/G peak intensity ratio of m-RGO/TiO<sub>2-x</sub>

compared with that in GO, suggesting a decrease tendency for the average size in the sp<sup>2</sup> domains in the reduced exfoliated GO. This could be explained by the fact that in size the sp<sup>2</sup> domains are relatively smaller than the ones which present in GO before reduction with new graphitic domains created.[51] The Raman measurements also show that hydrothermal reaction simultaneously promotes production of the Ti<sup>3+</sup> doping and the reduction of GO, which conforms to the XPS and XRD.

Furthermore, the fourier transform infrared (FTIR) spectra (Fig. 5d) of TiO<sub>2</sub>, GO and RGO/TiO<sub>2-x</sub> were obtained. After reaction, RGO/TiO<sub>2-x</sub> had a similar peak position to TiO<sub>2</sub>. The strong absorption peak at 479 cm<sup>-1</sup> was due to the Ti-O-Ti stretching vibration, indicating better combination of RGO and TiO<sub>2</sub>. Layers of graphite oxide contained many oxygen-containing surface functional groups, corresponding to the absorption peak of stretching vibration of -OH (3403 cm<sup>-1</sup>), the C=O stretching vibration in the carboxyl groups (1728 cm<sup>-1</sup>), the skeletal vibration bands of C=C (1626 cm<sup>-1</sup>), the C-OH deformation vibration peak (1390 cm<sup>-1</sup>), the stretching vibration band of C-O within C-OH (1238 cm<sup>-1</sup>) and stretching vibration peak of C-O in the epoxy groups (1072 cm<sup>-1</sup>), respectively.[40] Compared with GO, the vibration intensities of the main oxygen-containing functionality in RGO/TiO<sub>2-x</sub> composite corresponding to 1728、1390、1238 and 1072 cm<sup>-1</sup> were obviously weakened, which indicated that graphene oxide has been partially reduced during hydrothermal process.[52,53]

UV-vis diffuse reflectance spectroscopy (UV-DRS) studies of TiO<sub>2</sub>, TiO<sub>2-x</sub> and m-RGO/TiO<sub>2-x</sub> are shown in Fig. 6a, and reflected the different band gap structures and optical properties of photocatalytic materials. Pure TiO<sub>2</sub> absorbed only UV light, and its basic absorption edge was close to 400 nm as a result of charge transport from the valence band of O 2p to the conduction band of Ti 3d.[7,54] Compared with the original TiO<sub>2</sub>, the TiO<sub>2-x</sub> showed that the absorption between 400 and 800 nm was further

improved, and the absorption edge exhibited a palpable red shift in contrast to pristine  $\text{TiO}_2$ , which suggested that the band gap size of  $\text{TiO}_{2-x}$  was narrowed. Normally, the higher absorption intensity towards visible region indicates the better photocatalytic properties of photocatalysts.[7,60] As expected, the absorption intensity of m-RGO/ $\text{TiO}_{2-x}$  from 400 nm to 800 nm was further enhanced, suggesting that the photocatalytic properties of m-RGO/ $\text{TiO}_{2-x}$  was more optimal than that of  $\text{TiO}_2$  and  $\text{TiO}_{2-x}$ . The spectrum of 0.2-RGO+ $\text{TiO}_{2-x}$ , which was shown in Fig. S4, was investigated as a reference profile.

As shown in Fig. 6b, the photoluminescence (PL) analysis of  $\text{TiO}_2$ ,  $\text{TiO}_{2-x}$  and RGO/ $\text{TiO}_{2-x}$  were used to study the behavior of photogenerated electron-hole pairs, which was due to photoluminescence attributing to the electrons and holes recombination.[44] In general, the higher recombination rates of electrons and holes correspond to a greater PL spectra intensity. The band intensity of  $\text{TiO}_{2-x}$  was weaker than that of pure  $\text{TiO}_2$  which the peaks were distributed in the range of 400–600 nm, indicating that electron-hole pairs recombination efficiency of  $\text{TiO}_{2-x}$  was lower. After reaction with RGO, the PL intensity of the RGO/ $\text{TiO}_{2-x}$  further significantly decreased, which indicated the efficient interfacial electron transfer from conduction band of  $\text{TiO}_{2-x}$  to RGO to inhibit the photoinduced carrier recombination which was beneficial to photocatalysis. This result above was in general agreement with the UV-DRS.

### *3.1. Photoelectrochemical Performance*

For comparing the photoelectrochemical performance of  $\text{TiO}_{2-x}$  and m-RGO/ $\text{TiO}_{2-x}$  to that of  $\text{TiO}_2$ , the photocurrent response spectra (Fig. 7a) of the samples were collected which were recorded in 0.1 M  $\text{Na}_2\text{SO}_4$  under simulated sunlight irradiation via chronoamperometry technology. Photocurrent density was increases instantaneously when the light was turned on, and sharply decreased when the light was

turned off. The photocurrent intensity still kept steady and reproducible over several intermittent on-off cycle experiments under visible irradiation. Apparently, the photocurrent density of  $\text{TiO}_{2-x}$  was obviously enhanced under illumination, suggesting that the  $\text{TiO}_{2-x}$  had more effective charges separation and transportation, compared with pristine  $\text{TiO}_2$ . When the light was illuminated, the photocurrent intensity of pure  $\text{TiO}_2$  was about  $0.0006 \text{ mA cm}^{-1}$ . However, due to the doping of  $\text{Ti}^{3+}$ , the photocurrent value of  $\text{TiO}_{2-x}$  increased to  $0.0024 \text{ mA}\cdot\text{cm}^{-1}$  which was 4 times higher than that of pure  $\text{TiO}_2$ . The enhanced photocurrent density indicates more efficient separation of electron-hole and transportation of charges from valance band to conduction band in modified  $\text{TiO}_{2-x}$ , compared with pure  $\text{TiO}_2$ . The photocurrent density of m-RGO/ $\text{TiO}_{2-x}$  (m= 0.1, 0.2 and 0.3 g) were  $0.005 \text{ mA}\cdot\text{cm}^{-1}$ ,  $0.018 \text{ mA}\cdot\text{cm}^{-1}$ , and  $0.011 \text{ mA}\cdot\text{cm}^{-1}$ , which were about 8 times, 30 times and 18 times as high as the pristine  $\text{TiO}_2$  respectively. The relatively stronger photocurrent signals could be attributable to the cause that the decoration of RGO into the  $\text{TiO}_2$  system contributed to photo-induced electron transport from  $\text{TiO}_2$  to the surface of RGO. Similarly, the photocurrent density of 0.2-RGO+ $\text{TiO}_{2-x}$  (Fig. S5) was stable at  $0.005 \text{ mA}\cdot\text{cm}^{-1}$ , which is far below 0.2-RGO/ $\text{TiO}_{2-x}$ .

To further determine the properties of electron-transport and recombination of m-RGO/ $\text{TiO}_{2-x}$  over  $\text{TiO}_2$  and  $\text{TiO}_{2-x}$ , the electrochemical impedance spectra (EIS) measurements of all electrodes were investigated. It is generally known that the radius of the Nyquist circle is directly related to charge transfer resistance, with a smaller semicircle radius corresponding to easier the electron transfer.[55] As shown in Fig. 7b, the semicircle radius of  $\text{TiO}_{2-x}$  was smaller than that of  $\text{TiO}_2$ , indicating that  $\text{TiO}_{2-x}$  had better photo-generated electron-hole separation over  $\text{TiO}_2$ . Furthermore, the EIS Nyquist plot of m-RGO/ $\text{TiO}_{2-x}$  composites with different quantities of graphene oxide (0.1, 0.2 and 0.3 g) showed the smallest semicircular radius than  $\text{TiO}_2$  and  $\text{TiO}_{2-x}$ , which

suggested the faster interfacial electron transfer to electronic acceptor after combining with RGO, contributing to effective electron-hole separation. All consequences of photocurrent and EIS were consistent with the UV-DRS, which suggested that the Ti<sup>3+</sup> doping and the introduction of RGO were beneficial for facilitating the photo-induced electron-hole pairs separation and the electron transfer. These good properties bring about the photocatalytic performance.

Further, the photocurrent response of the TiO<sub>2-x</sub> and m-RGO/TiO<sub>2-x</sub> to that of TiO<sub>2</sub> were investigated by linear sweep voltammetry tests. The photocurrent density-potential curves under visible light exposure were presented in Fig. 7c. The corresponding values of m-RGO/TiO<sub>2-x</sub> all exceeded that of the TiO<sub>2</sub> and TiO<sub>2-x</sub>. The maximum photocurrent density of m-RGO/TiO<sub>2-x</sub> (m= 0.1, 0.2 and 0.3 g) were around 0.15 mA·cm<sup>-1</sup>, 0.34 mA·cm<sup>-1</sup> and 0.28 mA·cm<sup>-1</sup>, which were about 5 times, 11 times and 9 times as high as the pristine TiO<sub>2</sub> (about 0.03 mA·cm<sup>-1</sup>), respectively, meaning stronger ability of transporting charge carriers and separating electrons and holes in RGO/TiO<sub>2-x</sub> compound. Additionally, the initial potentials of m-RGO/TiO<sub>2-x</sub> composites were negatively shifted relative to pristine TiO<sub>2</sub>, implying that more electrons released and accumulated in the heterostructure and thus resulting in the electronegativity enhancement of anodic potentials.<sup>[56]</sup> The above results show that 0.2-RGO/TiO<sub>2-x</sub> composites exhibit excellent photoelectrochemical properties.

To compare the photoresponse performance of TiO<sub>2-x</sub> and 0.2-RGO/TiO<sub>2-x</sub> nanocomposites to simple TiO<sub>2</sub>, the incident photon-to-electron conversion efficiencies (IPCE) of these as-prepared photocatalysts were collected. The IPCE values were computed with the following formula (1):<sup>[56]</sup>

$$\text{IPCE (\%)} = \left( \frac{1240}{\lambda} \right) \times \left( \frac{J_{ph}}{J_{light}} \right) \times 100\% \quad (1)$$

where  $\lambda$  is the incident light wavelength (nm),  $J_{\text{ph}}$  is photocurrent density ( $\text{mA}\cdot\text{cm}^{-2}$ ), and  $I_{\text{light}}$  is the incident light power density ( $\text{mW}\cdot\text{cm}^{-2}$ ) for each wavelength. As can be noticed from Fig. 7d, the as-synthesized  $\text{TiO}_{2-x}$  and 0.2-RGO/ $\text{TiO}_{2-x}$  held higher IPCE values in visible region with wider range than original  $\text{TiO}_2$ , indicating the enhanced utilization of visible light for 0.2-RGO/ $\text{TiO}_{2-x}$  composites.

### 3.2. Photocatalytic performance

The photocatalytic ability of the  $\text{TiO}_2$ ,  $\text{TiO}_{2-x}$  and m-RGO/ $\text{TiO}_{2-x}$  was investigated by the decomposition of MB pollutant under simulated visible irradiation. Fig. 8a shows the photocatalytic rates under Xenon lamp irradiation. The MB solution concentration of used in the experiment was  $40 \text{ mg L}^{-1}$ , which was much higher than the concentration ( $10 \text{ mg L}^{-1}$ ) used in many of reported articles. Considering the possibility of self-degradation of MB by irradiation without catalyst, a blank experiment was tested as a benchmark. The result revealed that the photolysis of the MB was negligible on the experiment timetable. Before each photocatalytic reaction, adsorption–desorption experiment was established. After 12 h adsorption, the concentration of pollutants was basically unchanged, which indicated that the behavior of adsorption–desorption had reached a balance. Under simulated solar irradiation for 120 min, the photodegradation efficiency of pure  $\text{TiO}_2$  was only 35.4 % for MB removal due to poor visible light absorption intensity. The visible-light photodegradation rate of  $\text{TiO}_{2-x}$  increased to around 51.9 % after 120 min, indicating that the self-doping of  $\text{Ti}^{3+}$  contributed to the photocatalytic effect. However, with the combination of GO to  $\text{TiO}_{2-x}$ , its photodegradation activity further enhanced greatly. The photodegradation rates of m-RGO/ $\text{TiO}_{2-x}$  ( $m = 0.1, 0.2$  and  $0.3 \text{ g}$ ) in 120 min were 78.4 %, 98.3 % and 100 %, respectively, which could be in consequence of the coordination effect between RGO and the doping of  $\text{Ti}^{3+}$ . Fig. 8b displayed the UV-vis absorption spectra of MB (heavy

concentrations, 40 mg L<sup>-1</sup>) for 0.2- RGO/TiO<sub>2-x</sub> at intervals of irradiation time. The absorption peak of MB could be found, which clearly showed that the concentration of MB decreased with the progressive increase of time. For the sake of investigate thoroughly the photocatalytic activity of synthesized nanomaterials, the data of photocatalytic capacity were fitted, followed the pseudo-first-order kinetic equation (2):[58]

$$\ln \frac{C_t}{C_0} = kt \quad (2)$$

where  $C_0$ ,  $C_t$  and  $t$  are the initial MB concentration after adsorption equilibrium, concentration after a certain photodegradation reaction time and irradiation time, and the rate constant  $k$  is equivalent to appropriate slope of the computer fitting curve. The relation curves of  $\ln (C_0/C_t)$  vs. time were shown in Fig. S6. The value of rate constant  $k$  over TiO<sub>2</sub>, TiO<sub>2-x</sub> and m-RGO/TiO<sub>2-x</sub> are 0.00151, 0.00246, 0.00512, 0.01603 and 0.01958 min<sup>-1</sup> for MB, respectively, which are shown in Tables S1. **In addition to MB, the colorless organic contaminant, such as phenol, could also be degraded. Compared to TiO<sub>2</sub>, TiO<sub>2-x</sub>, the 0.2-RGO/TiO<sub>2-x</sub> has an excellent photodegradation rate for the elimination of phenol under simulated visible light (Fig. S7). Through the measurement of TOC analyser, the mineralization rate of MB over the m-RGO/TiO<sub>2-x</sub> can be up to 75.7%, 86.6 % and 89.4% within 120 min, respectively (Fig. S8). Due to the generation of organic intermediates during pollutant degradation process, the TOC degradation efficiency of MB are relatively lower than the degradation rates. Based on these results, it was demonstrated that the photodegradation activity of RGO/TiO<sub>2-x</sub> is all higher than TiO<sub>2</sub> photocatalysts. Furthermore, in order to better appraise photocatalytic property of RGO/TiO<sub>2-x</sub>, many reported photocatalysts are compared, which is listed in Table S2.**

For practical industrial applications in wastewater treatment, the recycling ability and stability of photocatalysts have an indispensable influence on the photodegradation

of pollutants. In order to explore the recyclability of photocatalysts, the photocatalyst was centrifuged and reused in repeated experiments five times under the same condition. As shown in Fig. 8c, the photodegradation performance of 0.2-RGO/TiO<sub>2-x</sub> did not have obvious reduction after the fourth cycle under 2 h of irradiation. Generally speaking, the as-prepared RGO/TiO<sub>2-x</sub> composite possesses excellent photocatalytic stability, performing as an environmental-friendly photocatalyst with a prospective application in sewage treatment. To further research the stability of prepared photocatalysts, XRD spectra of the TiO<sub>2</sub> and m-RGO/TiO<sub>2-x</sub> after the photo-degradation of MB were shown in Fig. S9. No obvious change occurred in the crystalline structures of the samples and no impurity peak was found, indicating that the m-RGO/TiO<sub>2-x</sub> are particularly stable after multiple photodegradation process. It is corresponding to the experiment of photocatalytic recyclability.

In order to deeply explore the photocatalytic mechanism of the RGO/TiO<sub>2-x</sub>, the active radical species produced in the process of photocatalysis were identified. The free radical capture and hole experiments were carried out by adding various scavengers including 1, 4-benzoquinone (BQ, as a O<sup>2•-</sup> scavenger), disodium ethylenediaminetetraacetate dihydrate (EDTA-2Na, as a h<sup>+</sup> scavenger) and isopropanol (IPA, as a •OH scavenger) as shown in Fig. 8d. The photocatalytic degradation efficiency of MB over 0.2-RGO/TiO<sub>2-x</sub> was basically unchanged in the presence of 10 mM of BQ, which proved the absence of O<sup>2•-</sup> radical group. However, after adding EDTA-2Na reagent as a h<sup>+</sup> scavenger, the degradation efficiency of MB was greatly suppressed. Additionally, the addition of IPA reduced the photocatalytic efficiency rate to 13%, suggesting that •OH radical species was crucial to the degradation of MB. These obtained results attested that the h<sup>+</sup> and •OH radical species have considerable influence on the photodegradation process of the RGO/TiO<sub>2-x</sub> composite.

Based on the above performance analysis, the photodegradation mechanism diagram of synthetic RGO/TiO<sub>2-x</sub> composite is shown in Scheme 2. A new sublevel state appears at the conduction band (CB) bottom of TiO<sub>2</sub>, which is put down to to the presence of the Ti<sup>3+</sup> and Ov. The mid-gap state synergistically makes the TiO<sub>2</sub> band gap narrow at the lower level, which is beneficial for the effective separation of electron–hole to further promote the photocatalytic degradation reaction. When the RGO/TiO<sub>2-x</sub> composite is irradiated by visible light, photogenerated electrons from the VB are stimulated to the CB state and/or the intermediate band gap state of TiO<sub>2-x</sub>, and the electropositive holes are left on the VB. In general, these photogenerated electrons and holes will quickly recombined and only a small portion of the electrons is involved in the photocatalytic test. Nevertheless, in our work, the photoinduced electrons on the TiO<sub>2-x</sub> CB are harder to return back to VB owing to the formation of the intermediate band gap states between the VB and the CB of TiO<sub>2-x</sub>, inhibiting the recombination of electron and hole more efficiently. Furthermore, after combining with RGO, the photogenerated active electrons on the CB state of TiO<sub>2-x</sub> are further transferred to the RGO surface, which further promotes the electron-hole separation. Meanwhile, the holes located on the VB of anatase TiO<sub>2-x</sub> react with hydroxide ions or water producing hydroxyl radicals (•OH), which will oxidize organic pollutant directly to transform to CO<sub>2</sub> and H<sub>2</sub>O owing to the potential on the VB which is quite negative than the potential which demands to oxidize the adsorbed H<sub>2</sub>O on the surface into •OH.[55]

All in all, the excellent photocatalytic activity of visible light of RGO/TiO<sub>2-x</sub> nanocomposites could be in virtue of the following reasons:

(1) Due to the introduction of Ti<sup>3+</sup> self-doping in RGO/TiO<sub>2-x</sub> composite, the absorption ability of visible light is obviously improved.

(2) In the RGO/TiO<sub>2-x</sub> system, RGO acts as the electron acceptor, which is responsible for charge separation and leaves more holes on the VB to obtain reactive species which will enhance the photocatalytic activity. Additionally, the existence of RGO can also strengthen visible-light absorption, leading to the substantial improvement of photocatalytic performance.

(3) The intermediate gap energy level is revealed between the valence band maximum (VBM) and the conduction band minimum (CBM) of TiO<sub>2-x</sub>, leading to the transfer of electrons either from VBM to a middle gap energy state or from a middle gap energy state to CBM more effectively. In this way, it is difficult for the electrons from CBM to move back to VBM, which hinders the corresponding charge recombination more efficiently.

#### **4. Conclusions**

In brief, we have luckily developed a visible-light active nanocomposite RGO/TiO<sub>2-x</sub> via a facile solvothermal approach, which realized self-doping of Ti<sup>3+</sup> and the partial reduction of graphene oxide simultaneously without any reducing agents added. The Ti<sup>3+</sup> self-doping and the combination of TiO<sub>2-x</sub> with RGO not only remarkably enhanced the visible-light absorption of samples but also produced some solitary energy levels between the CBM and VBM, and the interfacial electrons transfer between TiO<sub>2-x</sub> and RGO can promote the separation of electrons and holes. The results showed that all RGO/TiO<sub>2-x</sub> nanocomposites performed better under visible light at photodegrading organic pollutant simulate wastewater than the pure TiO<sub>2</sub>, and the concentration of MB is 40 mg L<sup>-1</sup>, which shows excellent photocatalytic performance compared with the concentration (10 mg L<sup>-1</sup>) used in previously reported articles. Regarding to photocatalytic ability of as-prepared photocatalysts, the RGO/TiO<sub>2-x</sub> (0.2 g GO, 120 min irradiation time) was found to be the optimum photocatalysis sample

which revealed a 2.8 times enhancement for MB photodegradation efficiency than pure TiO<sub>2</sub>. Moreover, the 0.2-RGO/TiO<sub>2-x</sub> has an excellent photodegradation rate for the elimination of phenol colorless organic pollutant under simulated visible light. This work provides a facile and environment-friendly technique for the synthesis of the RGO/TiO<sub>2-x</sub>, presenting practical applications in building TiO<sub>2</sub>-based catalysts.

### Acknowledgements

The authors thank the National Natural Science Foundation of China (21501127 and 51502185) for financial support of this work. S. H. Li acknowledges the financial support from the China Scholarship Council. Ivan P. Parkin marked the records for a UK-China linkage grant.

### References

- [1] N. S. Lewis, Toward cost-effective solar energy use, *Science* 315 (2007) 798-801.
- [2] C. Y. Mao, F. Zuo, Y. Hou, X. H. Bu, P. Y. Feng, In Situ Preparation of a Ti<sup>3+</sup> Self-Doped TiO<sub>2</sub> Film with Enhanced Activity as Photoanode by N<sub>2</sub>H<sub>4</sub> Reduction, *Angew. Chem. Int. Ed.* 53 (2014) 10485-10489.
- [3] S. Fu, Y. D. Liu, Y. Ding, X. Q. Du, F. Y. Song, R. Xiang, B. C. Ma, A mononuclear cobalt complex with an organic ligand acting as a precatalyst for efficient visible light-driven water oxidation, *Chem. Commun.* 50 (2014) 2167-2169.
- [4] C. L. Yu, G. Li, S. Kumar, K. Yang, R. C. Jin, Phase Transformation synthesis of novel Ag<sub>2</sub>O/Ag<sub>2</sub>CO<sub>3</sub> heterostructures with high visible light efficiency in photocatalytic degradation of pollutants, *Adv. Mater.* 26 (2014) 892-898.
- [5] Z. F. Jiang, W. M. Wan, W. Wei, K. M. Chen, H. M. Li, P. K. Wong, J. M. Xie, Gentle way to build reduced titanium dioxide nanodots integrated with graphite-like carbon spheres: From DFT calculation to experimental measurement, *Appl. Catal. B: Environ.* 204 (2017) 283-295.
- [6] J. S. Lee, K. H. You, C. B. Park, Highly Photoactive, Low bandgap TiO<sub>2</sub> nanoparticles wrapped by graphene, *Adv. Mater.* 24 (2012) 1084-1088.
- [7] M. Z. Ge, S. H. Li, J. Y. Huang, K. Q. Zhang, S. S. Al-Deyab, Y. K. Lai, TiO<sub>2</sub> nanotube

- arrays loaded with reduced graphene oxide films: facile hybridization and promising photocatalytic application, *J. Mater. Chem. A* 3 (2015) 3491-3499.
- [8] Z. P. Xing, W. Zhou, F. Du, L. L. Zhang, Z. Z. Lu, H. Zhang, W. Li, Facile synthesis of hierarchical porous TiO<sub>2</sub> ceramics with enhanced photocatalytic performance for micropolluted pesticide degradation, *ACS Appl. Mater. Interfaces* 6 (2014) 16653-16660.
- [9] Z. Q. Sun, J. H. Kim, Y. Zhao, F. Bijarbooneh, V. Malgras, Y. Lee, Y. M. Kang, S. X. Dou, rational design of 3D dendritic TiO<sub>2</sub> nanostructures with favorable architectures, *J. Am. Chem. Soc.* 133 (2011) 19314-19317.
- [10] M. Z. Ge, C. Y. Cao, S. H. Li, Y. X. Tang, L. N. Wang, N. Qi, J. Y. Huang, K. Q. Zhang, S. S. Al-Deyab, Y. K. Lai, In situ plasmonic Ag nanoparticle anchored TiO<sub>2</sub> nanotube arrays as visible-light-driven photocatalysts for enhanced water splitting, *Nanoscale* 8 (2016) 5226-5234.
- [11] J. S. Cai, J. Y. Huang, M. Z. Ge, J. Iocozzia, Z. Q. Lin, K. Q. Zhang, Y. K. Lai, Immobilization of Pt nanoparticles via rapid and reusable electropolymerization of dopamine on TiO<sub>2</sub> nanotube arrays for reversible SERS substrates and nonenzymatic glucose sensors, *Small* 13 (2017) 1604240.
- [12] K. Sasan, F. Zuo, Y. Wang, P. Y. Feng, Self-doped Ti<sup>3+</sup>-TiO<sub>2</sub> as a photocatalyst for the reduction of CO<sub>2</sub> into a hydrocarbon fuel under visible light irradiation, *Nanoscale* 7 (2015) 13369-13372.
- [13] Z. K. Zheng, B. B. Huang, J. B. Lu, Z. Y. Wang, X. Y. Qin, X. Y. Zhang, Y. Dai, M. H. Whangbo, Hydrogenated titania: synergy of surface modification and morphology improvement for enhanced photocatalytic activity, *Chem. Commun.* 48 (2012) 5733-5735.
- [14] Y. Shiraiishi, H. Hirakawa, Y. Togawa, Y. Sugano, S. Ichikawa, T. Hirai, Rutile Crystallites Isolated from Degussa (Evonik) P25 TiO<sub>2</sub>: Highly Efficient Photocatalyst for Chemoselective Hydrogenation of Nitroaromatics, *ACS Catal.* 3 (2013) 2318-2326.
- [15] S. C. Pillai, P. Periyat, R. George, D. E. McCormack, M. K. Seery, H. Hayden, J. Colreavy, D. Corr, S. J. Hinder, Synthesis of high-temperature stable anatase TiO<sub>2</sub> photocatalyst, *J. Phys. Chem. C* 111 (2007) 1605-1611.
- [16] R. Asahi, T. Morikawa, H. Irie, T. Ohwaki, Nitrogen-doped titanium dioxide as visible-light-sensitive photocatalyst: designs, developments, and prospects, *Chem. Rev.* 114 (2014) 9824-9852.
- [17] S. A. Ansari, M. M. Khan, M. O. Ansari, M. H. Cho, Nitrogen-doped titanium dioxide (N-doped TiO<sub>2</sub>) for visible light photocatalysis, *New J. Chem.* 40 (2016) 3000-3009.

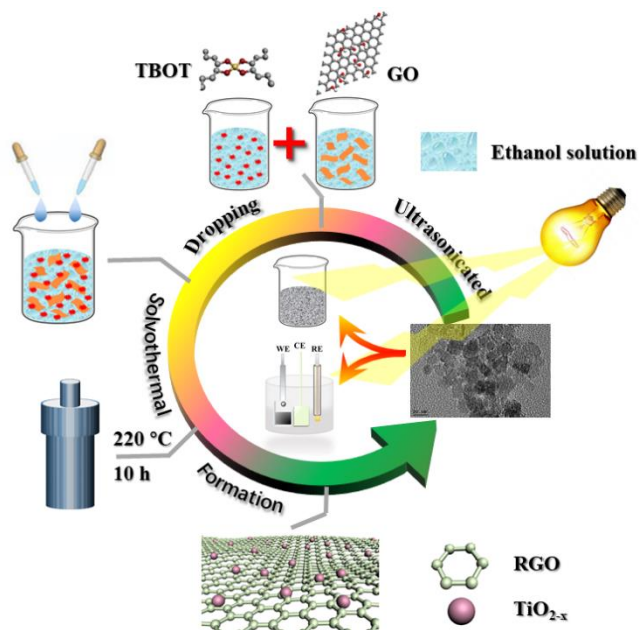
- [18] X. B. Chen, C. Burda, The electronic origin of the visible-light absorption properties of C-, N- and S-doped TiO<sub>2</sub> nanomaterials, *J. Am. Chem. Soc.* 130 (2008) 5018-5019.
- [19] A. Naldoni, M. Allieta, S. Santangelo, M. Marelli, F. Fabbri, S. Cappelli, C. L. Bianchi, R. Psaro, V. Dal Santo, Effect of nature and location of defects on bandgap narrowing in black TiO<sub>2</sub> nanoparticles, *J. Am. Chem. Soc.* 134 (2012) 7600-7603.
- [20] Y. Cao, Z. P. Xing, Y. C. Shen, Z. Z. Li, X. Wu, X. Yan, J. L. Zou, S. L. Yang, W. Zhou, Mesoporous black Ti<sup>3+</sup>/N-TiO<sub>2</sub> spheres for efficient visible-light-driven photocatalytic performance, *Chem. Eng. J.* 325 (2017) 199-207.
- [21] H. Y. Zhang, Y. F. Zhao, S. Chen, B. Yu, J. L. Xu, H. J. Xu, L. D. Hao, Z. M. Liu, Ti<sup>3+</sup> self-doped TiO<sub>x</sub>@anatase core-shell structure with enhanced visible light photocatalytic activity, *J. Mater. Chem. A* 1 (2013) 6138-6144.
- [22] X. B. Chen, L. Liu, P. Y. Yu, S. S. Mao, Increasing solar absorption for photocatalysis with black hydrogenated titanium dioxide nanocrystals, *Science* 331 (2011) 746-750.
- [23] H. Q. Lu, B. B. Zhao, R. L. Pan, J. F. Yao, J. H. Qiu, L. Luo, Y. C. Liu, Safe and facile hydrogenation of commercial Degussa P25 at room temperature with enhanced photocatalytic activity, *RSC Adv.* 4 (2014) 1128-1132.
- [24] Z. Wang, C. Y. Yang, T. Q. Lin, H. Yin, P. Chen, D. Y. Wan, F. F. Xu, F. Q. Huang, J. H. Lin, X. M. Xie, M. H. Jiang, Visible-light photocatalytic, solar thermal and photoelectrochemical properties of aluminium-reduced black titania, *Energy Environ. Sci* 6 (2013) 3007-3014.
- [25] Q. Kang, J. Y. Cao, Y. J. Zhang, L. Q. Liu, H. Xu, J. H. Ye, Reduced TiO<sub>2</sub> nanotube arrays for photoelectrochemical water splitting, *J. Mater. Chem. A* 1 (2013) 5766-5774.
- [26] C. Xu, Y. Song, L. F. Lu, C. W. Cheng, D. F. Liu, X. H. Fang, X. Y. Chen, X. F. Zhu, D. D. Li, Electrochemically hydrogenated TiO<sub>2</sub> nanotubes with improved photoelectrochemical water splitting performance, *Nanoscale Res. Lett.* 8 (2013).
- [27] S. Hoang, S. P. Berglund, N. T. Hahn, A. J. Bard, C. B. Mullins, Enhancing Visible Light Photo-oxidation of Water with TiO<sub>2</sub> Nanowire Arrays via Cotreatment with H<sub>2</sub> and NH<sub>3</sub>: Synergistic Effects between Ti<sup>3+</sup> and N, *J. Am. Chem. Soc.* 134 (2012) 3659-3662.
- [28] Y. G. Wang, D. C. Cantu, M. S. Lee, J. Li, V. A. Glezakou, R. Rousseau, CO oxidation on Au/TiO<sub>2</sub>: condition-dependent active sites and mechanistic pathways, *J. Am. Chem. Soc.* 138 (2016) 10467-10476.
- [29] L. Artiglia, S. Agnoli, A. Vittadini, A. Verdini, A. Cossaro, L. Floreano, G. Granozzi, Atomic structure and special reactivity toward methanol oxidation of vanadia nanoclusters on TiO<sub>2</sub>(110), *J. Am. Chem. Soc.* 135 (2013) 17331-17338.

- [30] Z. F. Bian, T. Tachikawa, P. Zhang, M. Fujitsuka, T. Majima, Au/TiO<sub>2</sub> superstructure-based plasmonic photocatalysts exhibiting efficient charge separation and unprecedented activity, *J. Am. Chem. Soc.* 136 (2014) 458-465.
- [31] Y. Xiong, J. F. Ian, Y. L. Cao, X. P. Ai, H. X. Yang, Electrospun TiO<sub>2</sub>/C nanofibers as a high-capacity and cycle-stable anode for Sodium-Ion batteries, *ACS Appl. Mater. Interfaces* 8 (2016) 16684-16689.
- [32] W. Teng, X. Y. Li, Q. D. Zhao, G. H. Chen, Fabrication of Ag/Ag<sub>3</sub>PO<sub>4</sub>/TiO<sub>2</sub> heterostructure photoelectrodes for efficient decomposition of 2-chlorophenol under visible light irradiation, *J. Mater. Chem. A* 1 (2013) 9060-9068.
- [33] Z. Wang, C. Y. Yang, T. Q. Lin, H. Yin, P. Chen, D. Y. Wan, F. F. Xu, F. Q. Huang, J. H. Lin, X. M. Xie, M. H. Jiang, H-Doped black titania with very high solar absorption and excellent photocatalysis enhanced by localized surface plasmon resonance, *Adv. Funct. Mater.* 23 (2013) 5444-5450.
- [34] J. Q. Pan, Y. Z. Sheng, J. X. Zhang, J. M. Wei, P. Huang, X. Zhang, B. X. Feng, Preparation of carbon quantum dots/TiO<sub>2</sub> nanotubes composites and their visible light catalytic applications, *J. Mater. Chem. A* 2 (2014) 18082-18086.
- [35] J. T. W. Wang, J. M. Ball, E. M. Barea, A. Abate, J. A. Alexander-Webber, J. Huang, M. Saliba, I. Mora-Sero, J. Bisquert, H. J. Snaith, R. J. Nicholas, Low-temperature processed electron collection layers of graphene/TiO<sub>2</sub> nanocomposites in thin film perovskite solar cells, *Nano Lett.* 14 (2014) 724-730.
- [36] S. A. Mu, Y. Z. Long, S. Z. Kang, J. Mu, Surface modification of TiO<sub>2</sub> nanoparticles with a C<sub>60</sub> derivative and enhanced photocatalytic activity for the reduction of aqueous Cr(VI) ions, *Catal. Commun.* 11 (2010) 741-744.
- [37] S. D. Perera, R. G. Mariano, K. Vu, N. Nour, O. Seitz, Y. Chabal, K. J. Balkus, Hydrothermal synthesis of graphene-TiO<sub>2</sub> nanotube composites with enhanced photocatalytic activity, *ACS Catal.* 2 (2012) 949-956.
- [38] A. K. Geim, Graphene: Status and Prospects, *Science* 324 (2009) 1530-1534.
- [39] X. Pan, Y. Zhao, S. Liu, C. L. Korzeniewski, S. Wang, Z. Y. Fan, Comparing graphene-TiO<sub>2</sub> nanowire and graphene-TiO<sub>2</sub> nanoparticle composite photocatalysts, *ACS Appl. Mater. Interfaces* 4 (2012) 3944-3950.
- [40] S. Y. Pu, R. X. Zhu, H. Ma, D. L. Deng, X. J. Pei, F. Qi, W. Chu, Facile in-situ design strategy to disperse TiO<sub>2</sub> nanoparticles on graphene for the enhanced photocatalytic degradation of rhodamine 6G, *Appl. Catal. B: Environ.* 218 (2017) 208-219.
- [41] N. Li, G. Liu, C. Zhen, F. Li, L. L. Zhang, H. M. Cheng, Battery Performance and photocatalytic activity of mesoporous anatase TiO<sub>2</sub> nanospheres/graphene composites

- by template-free self-assembly, *Adv. Funct. Mater.* 21 (2011) 1717-1722.
- [42] G. Williams, B. Seger, P.V. Kamat, TiO<sub>2</sub>-graphene nanocomposites. UV-assisted photocatalytic reduction of graphene oxide, *ACS Nano* 2 (2008) 1487-1491.
- [43] M. Y. Xing, W. Z. Fang, M. Nasir, Y. F. Ma, J. L. Zhang, M. Anpo, Self-doped Ti<sup>3+</sup>-enhanced TiO<sub>2</sub> nanoparticles with a high-performance photocatalysis, *J. Catal.* 297 (2013) 236-243.
- [44] K. Li, S. M. Gao, Q. Y. Wang, H. Xu, Z. Y. Wang, B. B. Huang, Y. Dai, J. Lu, In-situ-reduced synthesis of Ti<sup>3+</sup> self-doped TiO<sub>2</sub>/g-C<sub>3</sub>N<sub>4</sub> heterojunctions with high photocatalytic performance under LED light irradiation, *ACS Appl. Mater. Interfaces* 7 (2015) 9023-9030.
- [45] L. H. Li, L. L. Yu, Z. Y. Lin, G. W. Yang, Reduced TiO<sub>2</sub>-graphene oxide heterostructure as broad spectrum-driven efficient water-splitting photocatalysts, *ACS Appl. Mater. Interfaces* 8 (2016) 8536-8545.
- [46] R. Boppella, J. E. Lee, F. M. Mota, J. Y. Kim, Z. X. Feng, D. H. Kim, Composite hollow nanostructures composed of carbon-coated Ti<sup>3+</sup> self-doped TiO<sub>2</sub>-reduced graphene oxide as an efficient electrocatalyst for oxygen reduction, *J. Mater. Chem. A* 5 (2017) 7072-7080.
- [47] C. Wang, D. L. Meng, J. H. Sun, J. Memon, Y. Huang, J. X. Geng, Graphene wrapped TiO<sub>2</sub> based catalysts with enhanced photocatalytic activity, *Adv. Mater. Interfaces* 1 (2014) 1300150.
- [48] J. J. Mao, M. Z. Ge, J. Y. Huang, Y. K. Lai, C. J. Lin, K. Q. Zhang, K. Meng, Y. X. Tang, Constructing multifunctional MOF@rGO hydro-/aerogels by the self-assembly process for customized water remediation, *J. Mater. Chem. A* 5 (2017) 11873-11881.
- [49] B. J. Jiang, Y. Q. Tang, Y. Qu, J. Q. Wang, Y. Xie, C. G. Tian, W. Zhou, H. G. Fu, Thin carbon layer coated Ti<sup>3+</sup>-TiO<sub>2</sub> nanocrystallites for visible-light driven photocatalysis, *Nanoscale* 7 (2015) 5035-5045.
- [50] X. H. Wang, J. G. Li, H. Kamiyama, M. Katada, N. Ohashi, Y. Moriyoshi, T. Ishigaki, Pyrogenic Iron(III)-doped TiO<sub>2</sub> nanopowders synthesized in RF thermal plasma: Phase formation, defect structure, band gap, and magnetic properties, *J. Am. Chem. Soc.* 127 (2005) 10982-10990.
- [51] S. Stankovich, D. A. Dikin, R.D. Piner, K. A. Kohlhaas, A. Kleinhammes, Y. Y. Jia, Y. Wu, S. T. Nguyen, R. S. Ruoff, Synthesis of graphene-based nanosheets via chemical reduction of exfoliated graphite oxide, *Carbon* 45 (2007) 1558-1565.
- [52] Y. Xu, H. Bai, G. W. Lu, C. Li, G. Q. Shi, Flexible graphene films via the filtration of water-soluble noncovalent functionalized graphene sheets, *J. Am. Chem. Soc.* 130

(2008) 5856-5857.

- [53] H. L. Guo, X. F. Wang, Q. Y. Qian, F. B. Wang, X. H. Xia, A Green Approach to the synthesis of graphene nanosheets, *ACS Nano* 3 (2009) 2653-2659.
- [54] X. B. Chen, L. Liu, F. Q. Huang, Black titanium dioxide (TiO<sub>2</sub>) nanomaterials, *Chem. Soc. Rev.* 44 (2015) 1861-1885.
- [55] J. S. Cai, J. Y. Huang, Y. K. Lai, 3D Au-decorated BiMoO<sub>6</sub> nanosheet/TiO<sub>2</sub> nanotube array heterostructure with enhanced UV and visible-light photocatalytic activity, *J. Mater. Chem. A* 5 (2017) 16412-16421.
- [56] Q. Wang, J. Y. Huang, H. T. Sun, K. Q. Zhang, Y. K. Lai, MoS<sub>2</sub> quantum dots@TiO<sub>2</sub> nanotube arrays: An extended spectrum-driven photocatalyst for solar hydrogen evolution, *ChemSusChem*. 11 (2018) 1708-1721.
- [57] Y. X. Deng, M. Y. Xing, J. L. Zhang, An advanced TiO<sub>2</sub>/Fe<sub>2</sub>TiO<sub>5</sub>/Fe<sub>2</sub>O<sub>3</sub> triple-heterojunction with enhanced and stable visible-light-driven fenton reaction for the removal of organic pollutants, *Appl. Catal. B: Environ.* 211 (2017) 157–166.
- [58] M. Y. Xing, W. J. Xu, C. C. Dong, Y. C. Bai, J. B. Zeng, Y. Zhou, J. L. Zhang, Y. D. Yin, Metal sulfides as excellent co-catalysts for H<sub>2</sub>O<sub>2</sub> decomposition in advanced oxidation processes, *Chem.* 4 (2018) 1359-1372.
- [59] C. Y. Dong, C. Lian, S. C. Hu, Z. S. Deng, J. Q. Gong, M. D. Li, H. L. Liu, M. Y. Xing, J. L. Zhang, Size-dependent activity and selectivity of carbon dioxide photocatalytic reduction over platinum nanoparticles, *Nat. Commun.* 9 (2018) 1252.
- [60] M. Y. Xing, Y. Zhou, C. Y. Dong, L. J. Cai, L. X. Zeng, B. Shen, L. H. Pan, C. C. Dong, Y. Chai, J. L. Zhang, Y. D. Yin, Modulation of the reduction potential of TiO<sub>2-x</sub> by fluorination for efficient and selective CH<sub>4</sub> generation from CO<sub>2</sub> photoreduction, *Nano Lett.* 18 (2018) 3384–3390.



**Scheme 1.** Schematic diagram for preparation of m-RGO/TiO<sub>2-x</sub> and the corresponding photoelectrochemical characterization.

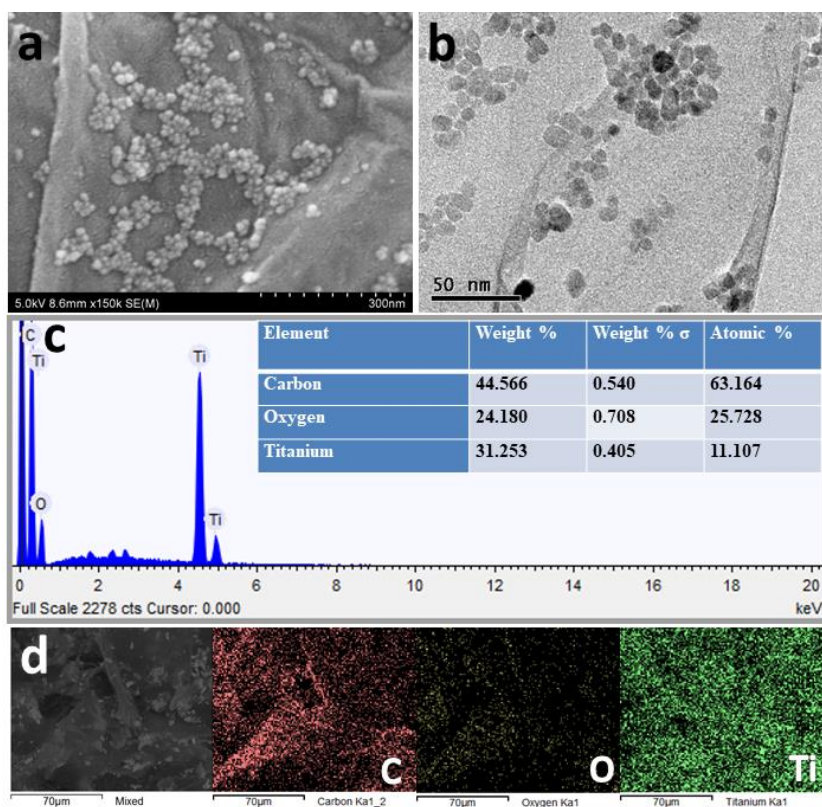


**Fig. 1.** FESEM (a) and TEM (b) of 0.2-RGO/TiO<sub>2-x</sub>. The corresponding EDS spectrum (c) and area element mapping (d) of 0.2-RGO/TiO<sub>2-x</sub>.

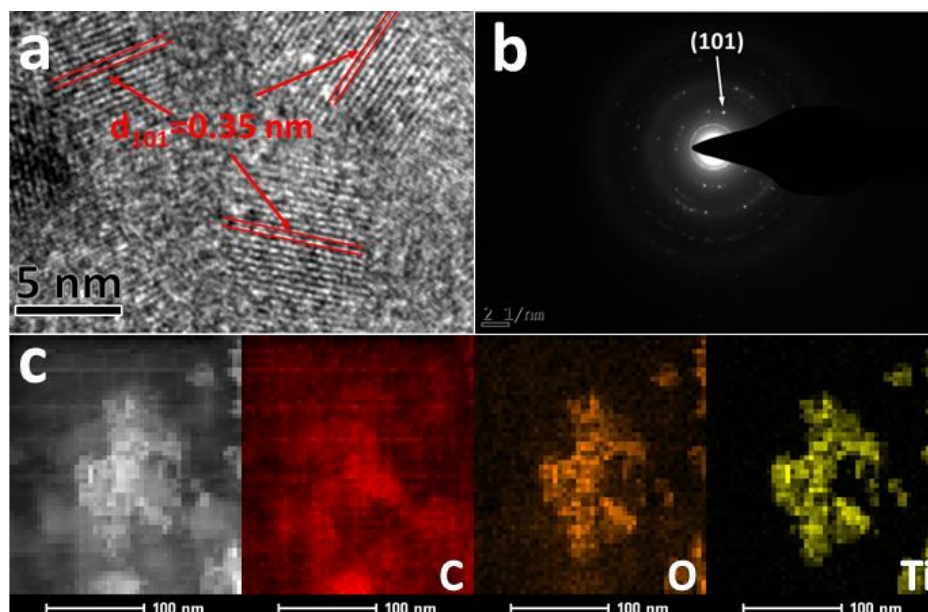


**Fig. 2.** HRTEM images (a) and the SAED pattern (b) of 0.2-RGO/TiO<sub>2-x</sub>. The corresponding narrow EDX element mapping (c) of 0.2-RGO/TiO<sub>2-x</sub>.

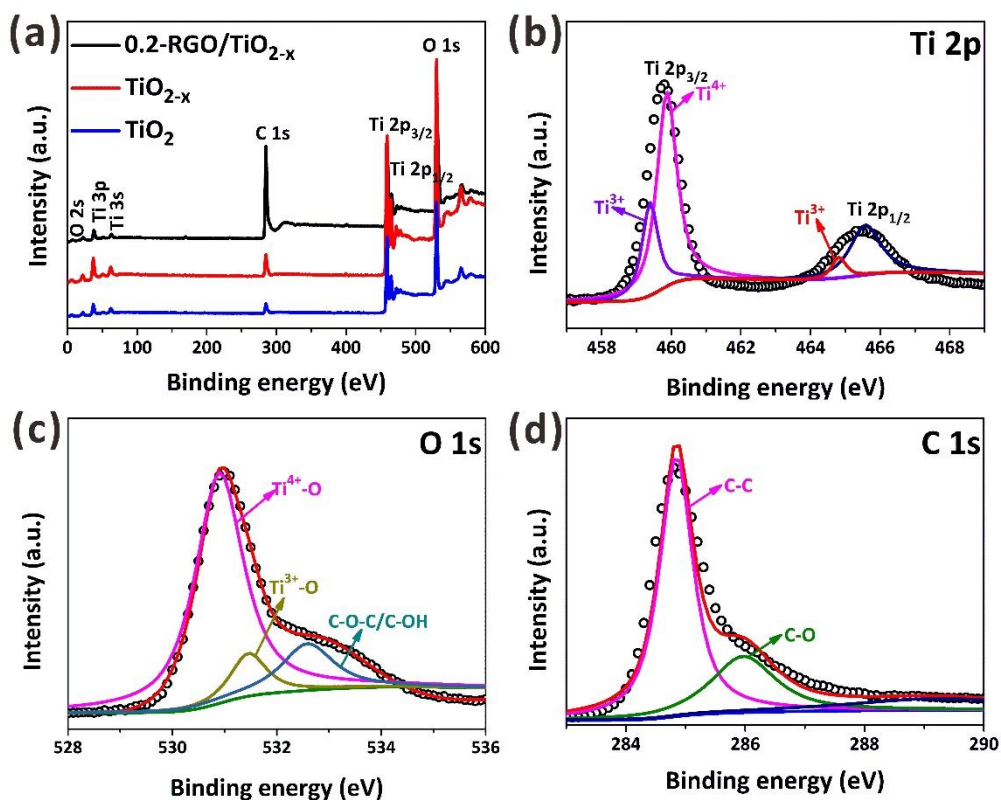


**Fig. 3.** XPS wide spectra of pure TiO<sub>2</sub>, TiO<sub>2-x</sub> and 0.2-RGO/TiO<sub>2-x</sub> (a) and the high resolution XPS spectra of Ti 2p (b), O 1s (c) and C 1s (d) for the as-prepared sample of 0.2-RGO/TiO<sub>2-x</sub>.

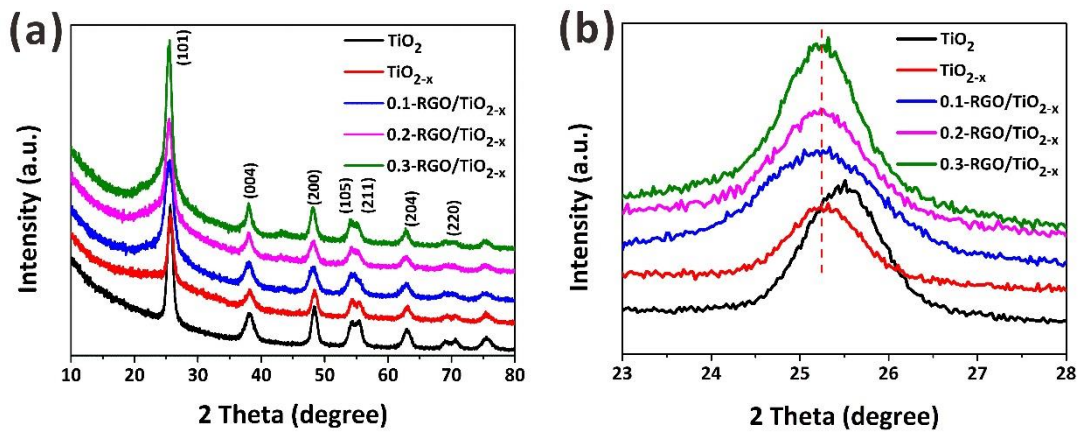


Fig. 4. XRD patterns of pristine  $\text{TiO}_2$ ,  $\text{TiO}_{2-x}$  and m-RGO/ $\text{TiO}_{2-x}$  (a and b).

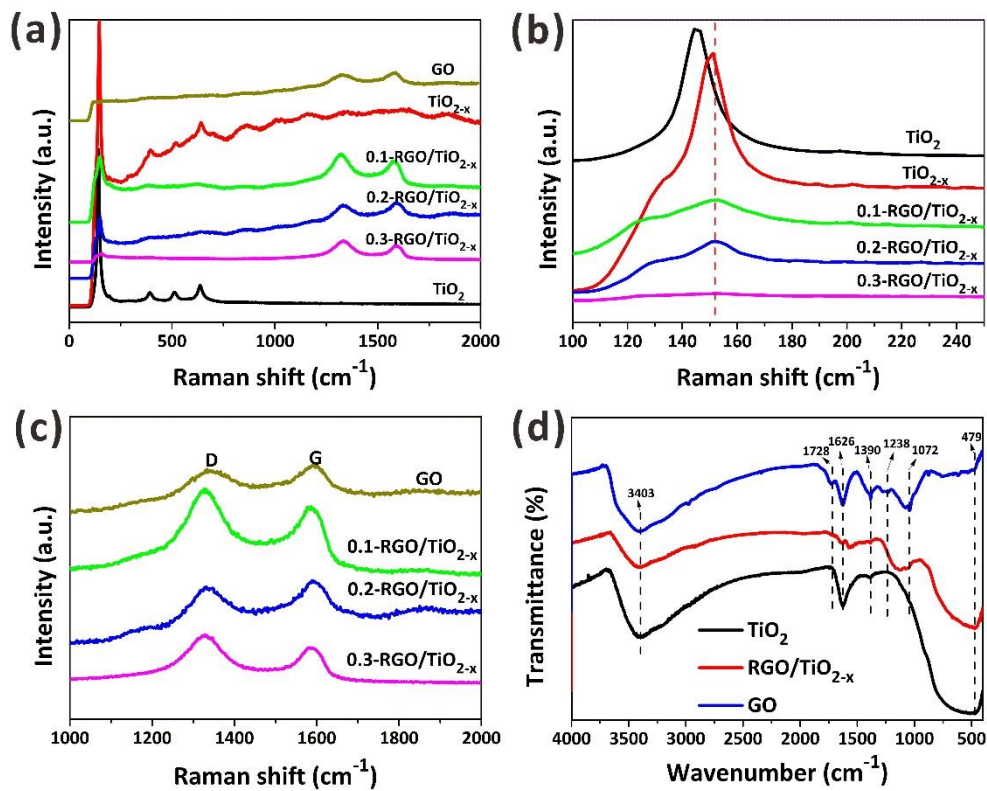
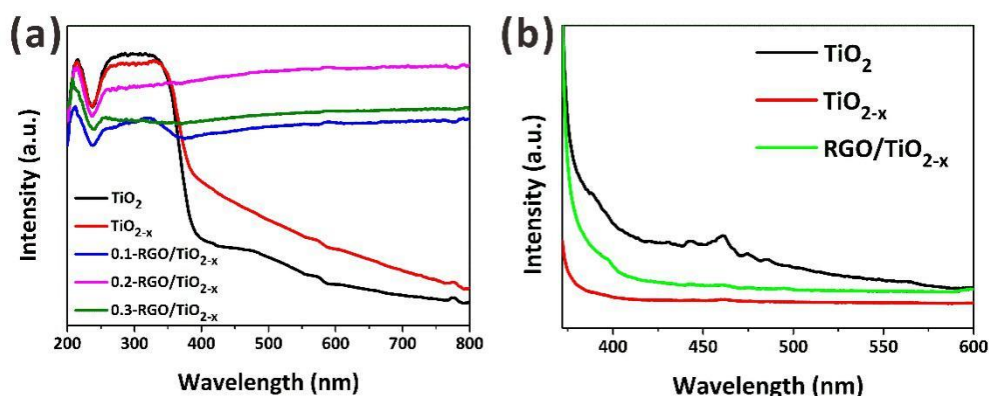
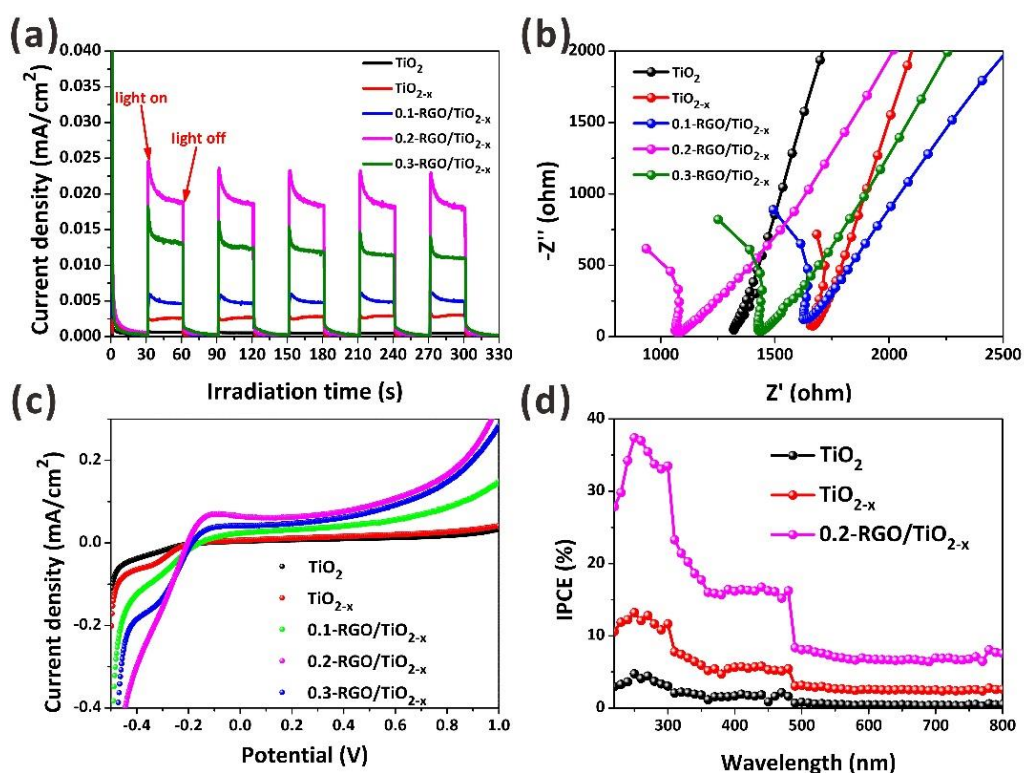


Fig. 5. Raman spectra (a) of GO,  $\text{TiO}_2$ ,  $\text{TiO}_{2-x}$  and m-RGO/ $\text{TiO}_{2-x}$ , the enlarged Raman spectra (b) of the peak ( $142.5 \text{ cm}^{-1}$ ) of  $\text{TiO}_2$ ,  $\text{TiO}_{2-x}$  nanoparticles and m-RGO/ $\text{TiO}_{2-x}$  compounds, and the enlarged Raman spectra (c) of the D ( $1326 \text{ cm}^{-1}$ ) and G ( $1582 \text{ cm}^{-1}$ ) bands of GO and m-RGO/ $\text{TiO}_{2-x}$ . FTIR spectra (d) of  $\text{TiO}_2$ , GO and 0.2-RGO/ $\text{TiO}_{2-x}$ .



**Fig. 6.** UV-DRS absorption spectra (a) of the pure  $\text{TiO}_2$ ,  $\text{TiO}_{2-x}$  and as-synthesized m-RGO/ $\text{TiO}_{2-x}$ . Photoluminescence spectra (b) of the pure  $\text{TiO}_2$ ,  $\text{TiO}_{2-x}$  and 0.2-RGO/ $\text{TiO}_{2-x}$ .



**Fig. 7.** Photocurrent responses spectroscopy (a), electrochemical impedance spectroscopy (EIS) (b) and photocurrent densities versus voltage curves (c) of the pure  $\text{TiO}_2$ ,  $\text{TiO}_{2-x}$  and as-synthesized m-RGO/ $\text{TiO}_{2-x}$ . Incident photon to current conversion efficiency (IPCE) curves (d) of the pure  $\text{TiO}_2$ ,  $\text{TiO}_{2-x}$  and as-prepared 0.2-RGO/ $\text{TiO}_{2-x}$ .

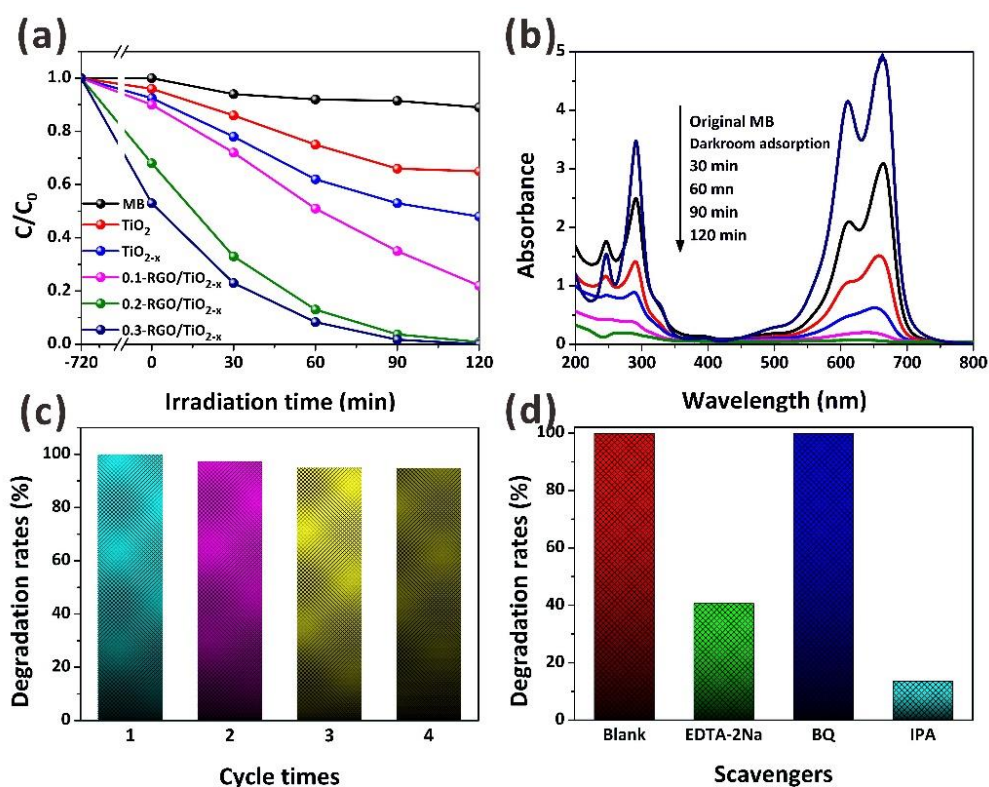
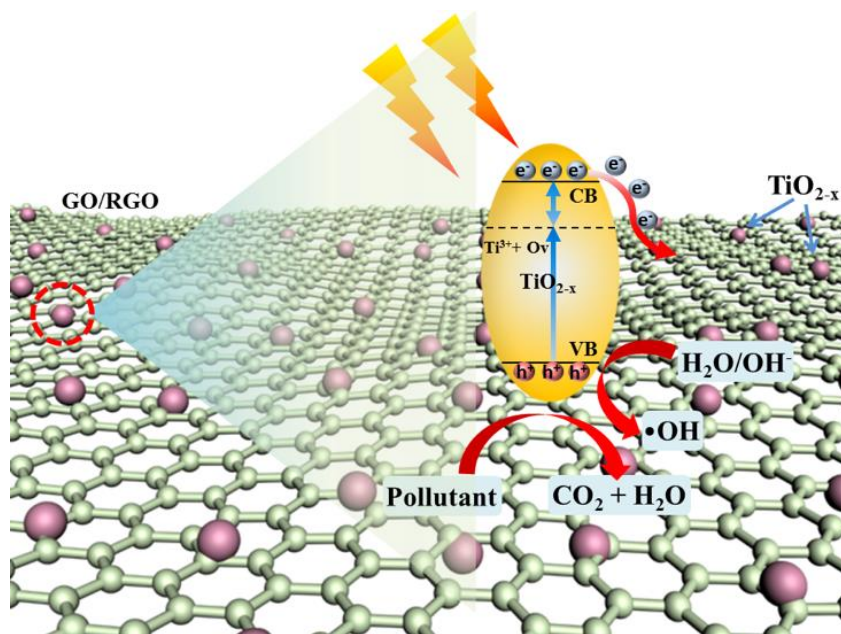
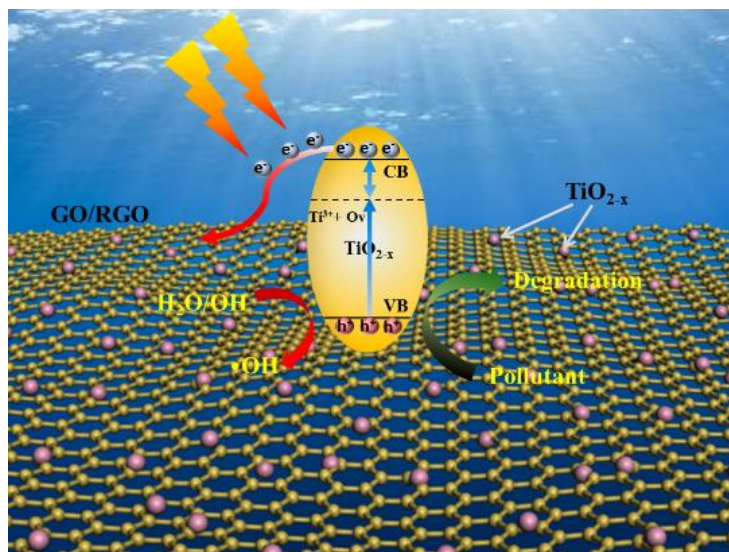


**Fig. 8.** Photodegradation efficiency (a) of MB (40 mg L<sup>-1</sup>) under effective visible-light irradiation for 120 min on the TiO<sub>2</sub>, TiO<sub>2-x</sub> and m-RGO/TiO<sub>2-x</sub>. UV-vis absorbance (b) of MB with certain irradiation time using the 0.2-RGO/TiO<sub>2-x</sub> under visible light. The reusability of 0.2-RGO/TiO<sub>2-x</sub> for photodegradation of MB with 4 times of cycling operation (c). Influence of different scavengers during photodegradation of MB pollutants in the presence of the 0.2-RGO/TiO<sub>2-x</sub> under ultraviolet irradiation (d).



**Scheme 2.** Schematic diagram of possible reaction mechanism of photodegradation process.

ToC figure



## Supporting Information

**Defective black Ti<sup>3+</sup> self-doped TiO<sub>2</sub> and reduced graphene oxide  
composite nanoparticles for boosting visible-light driven  
photocatalytic and photoelectrochemical activity**

*Shanchi Wang,<sup>a</sup> Jingsheng Cai,<sup>a</sup> Jiajun Mao,<sup>a</sup> Shuhui Li,<sup>ab</sup> Jiali Shen,<sup>a</sup> Shouwei Gao,<sup>a</sup>  
Jianying Huang,<sup>a</sup> Xiaoqin Wang,<sup>a</sup> Ivan P. Parkin,<sup>b</sup> Yuekun Lai,<sup>\*a</sup>*

a. National Engineering Laboratory for Modern Silk, College of Textile and Clothing Engineering, Soochow University, Suzhou 215123, P. R. China.

b. Materials Chemistry Research Centre, Department of Chemistry, University College London, London, UK

\*Correspondence to: Yuekun Lai (E-mail: [yklai@suda.edu.cn](mailto:yklai@suda.edu.cn))

**Figure Captions:**

**Table S1.** K values of the TiO<sub>2</sub>, TiO<sub>2-x</sub> and m-RGO/TiO<sub>2-x</sub> nanocomposites for degrading MB under visible light

**Fig. S1.** XPS spectra of Ti 2p (a) and O 1s (b) for the as-synthesized TiO<sub>2</sub> and 0.2-RGO/TiO<sub>2-x</sub>.

**Fig. S2.** XRD pattern of GO.

**Fig. S3.** XRD pattern (a and b) of TiO<sub>2</sub> and 0.2-RGO+ TiO<sub>2-x</sub>.

**Fig. S4.** UV-DRS absorption spectra of 0.2-RGO/TiO<sub>2-x</sub> and 0.2-RGO+TiO<sub>2-x</sub>.

**Fig. S5.** Photocurrent responses of 0.2-RGO+TiO<sub>2-x</sub>.

**Fig. S6.** Photocatalytic activity towards the degradation of MB with the  $\text{TiO}_2$ ,  $\text{TiO}_{2-x}$  and m-RGO/ $\text{TiO}_{2-x}$  nanocomposites under visible light irradiation.

**Fig. S7.** Photodegradation efficiency of phenol ( $10 \text{ mg L}^{-1}$ ) under effective visible-light irradiation for 150 min on the  $\text{TiO}_2$ ,  $\text{TiO}_{2-x}$  and 0.2-RGO/ $\text{TiO}_{2-x}$ .

**Fig. S8.** Mineralization rates of MB by the samples under visible light irradiation. Samples 1–5 denote  $\text{TiO}_2$ ,  $\text{TiO}_{2-x}$  and m-RGO/ $\text{TiO}_{2-x}$ , respectively.

**Fig. S9.** XRD patterns of the  $\text{TiO}_2$  and m-RGO/ $\text{TiO}_{2-x}$  after the photo-degradation of MB.

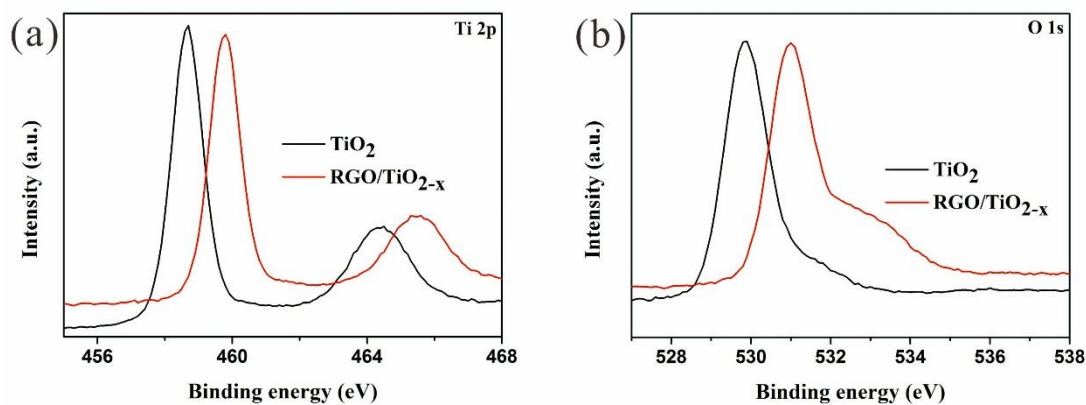


**Fig. S1.** XPS spectra of Ti 2p (a) and O 1s (b) for the as-synthesized  $\text{TiO}_2$  and 0.2-RGO/ $\text{TiO}_{2-x}$ .

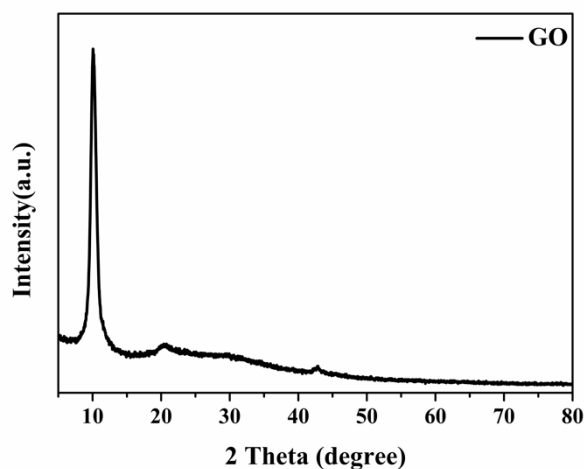


**Fig. S2.** XRD pattern of GO.

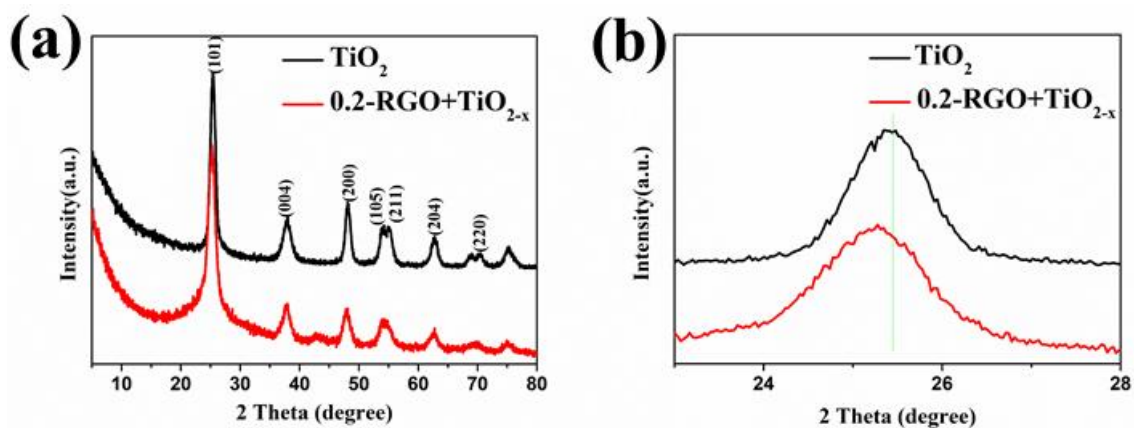


Fig. S3. XRD pattern (a and b) of  $\text{TiO}_2$  and  $0.2\text{-RGO}+\text{TiO}_{2-x}$ .

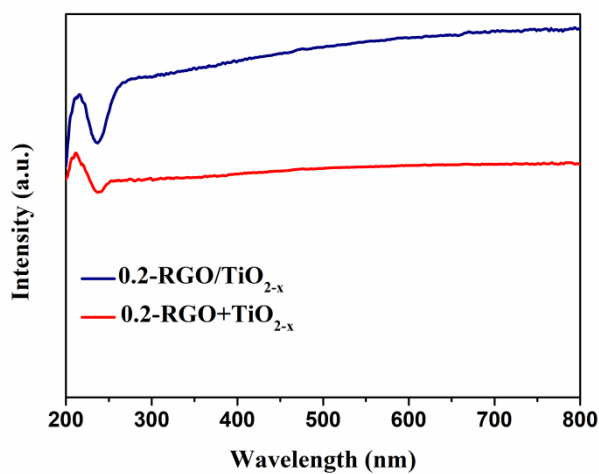


Fig. S4. UV-DRS absorption spectra of  $0.2\text{-RGO}/\text{TiO}_{2-x}$  and  $0.2\text{-RGO}+\text{TiO}_{2-x}$ .

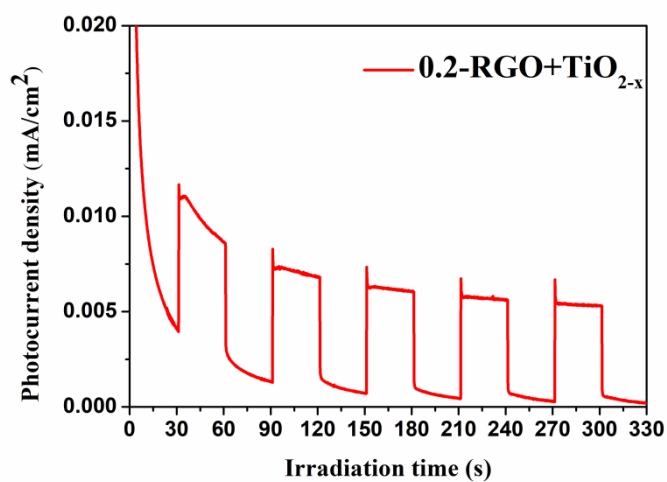
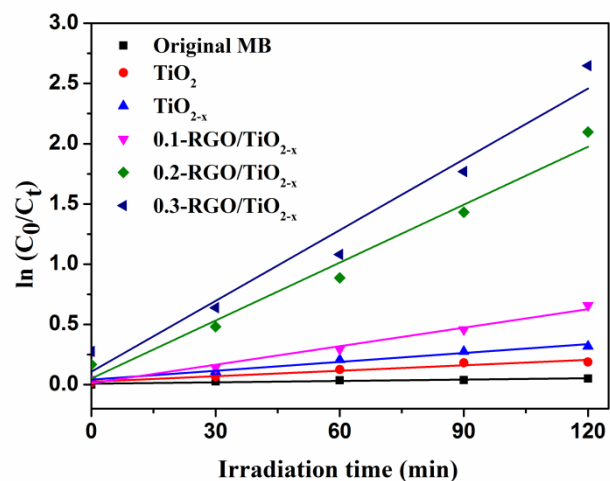
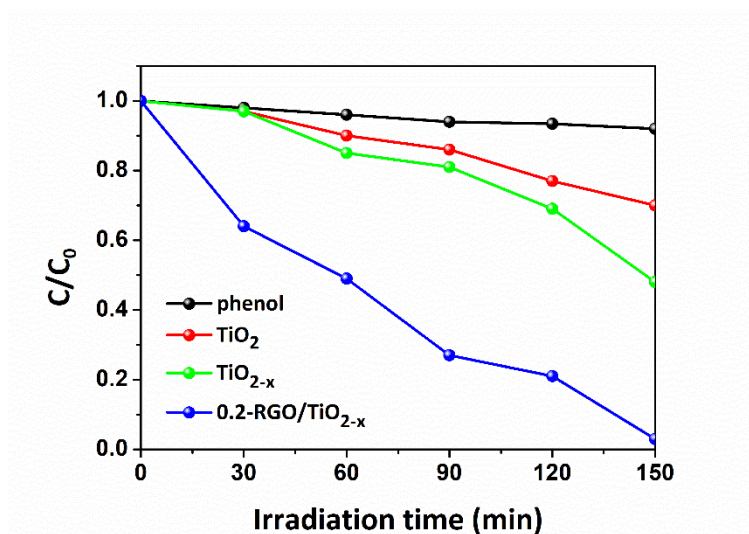


Fig. S5. Photocurrent responses of  $0.2\text{-RGO}+\text{TiO}_{2-x}$ .



**Fig. S6.** Photocatalytic activity towards the degradation of MB with the TiO<sub>2</sub>, TiO<sub>2-x</sub> and m-RGO/TiO<sub>2-x</sub> nanocomposites under visible light irradiation.



**Fig. S7.** Photodegradation efficiency of phenol (10 mg L<sup>-1</sup>) under effective visible-light irradiation for 150 min on the TiO<sub>2</sub>, TiO<sub>2-x</sub> and 0.2-RGO/TiO<sub>2-x</sub>.

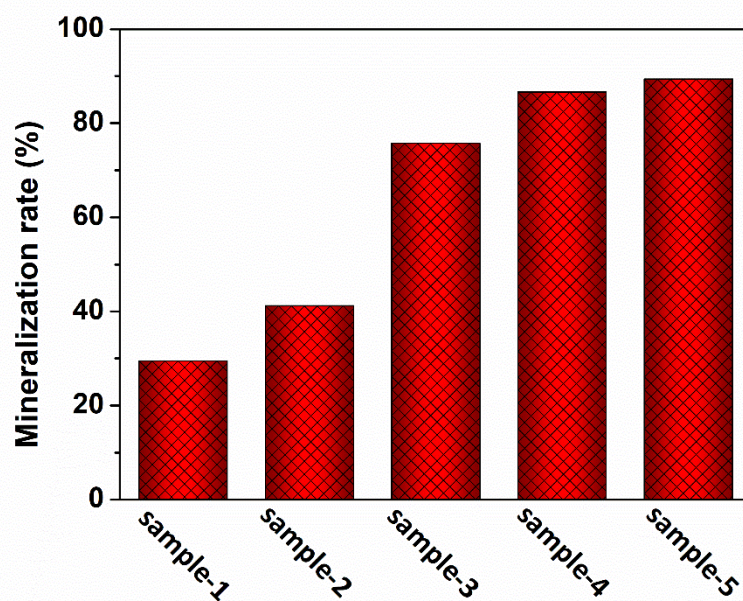


**Fig. S8.** Mineralization rates of MB by the samples under visible light irradiation. Samples 1–5 denote  $\text{TiO}_2$ ,  $\text{TiO}_{2-x}$  and m-RGO/ $\text{TiO}_{2-x}$ , respectively.

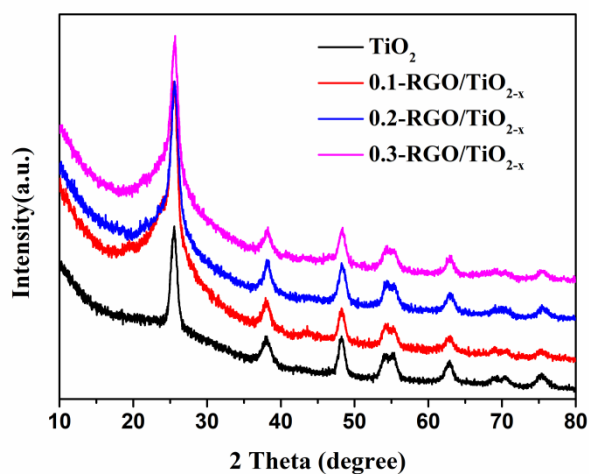


**Fig. S9.** XRD patterns of the  $\text{TiO}_2$  and m-RGO/ $\text{TiO}_{2-x}$  after the photo-degradation of MB.

**Table S1.** K values of the TiO<sub>2</sub>, TiO<sub>2-x</sub> and m-RGO/TiO<sub>2-x</sub> nanocomposites for degrading MB under visible light

Samples	TiO <sub>2</sub>	TiO <sub>2-x</sub>	0.1-RGO/TiO <sub>2-x</sub>	0.2-RGO/TiO <sub>2-x</sub>	0.3-RGO/TiO <sub>2-x</sub>
<b>K (min<sup>-1</sup>)</b>	0.00151	0.00246	0.00512	0.01603	0.01958

**Table S1.** Comparison of the photocatalytic performance for degradation of MB.

Photocatalyst	Light sources	Catalyst amount vs. MB Conc & Vol	Photodegradation efficiency vs. reaction time	Rate constant	Ref.
RGO/TiO <sub>2-x</sub>	500 W Xe lamp	50 mg vs. 50 ml of 40 mg/L	100%--120 min	0.01958 min <sup>-1</sup>	This work
CuO@CSH	300 W Xe lamp	20 mg vs. 50 ml of 20 mg/L	90%--150 min	0.0119 min <sup>-1</sup>	1
ZIF-8/rGA	300 W mercury lamp	0.5 g/L vs. 100 ml of 25 mg/L	51.8%--120 min	0.00432 min <sup>-1</sup>	2
mpg-C <sub>3</sub> N <sub>4</sub> /SnCoS <sub>4</sub>	300 W Xe lamp	20 mg vs. 100 ml of 20 mg/L	95%--160 min	0.01374 min <sup>-1</sup>	3
BN-Ag/TiO <sub>2</sub>	> 400 nm	0.4 g/L vs. 20 mg/L	98%--80 min	0.0465 min <sup>-1</sup>	4
LP(Ti)	500 W Xe lamp	5 mg vs. 40 ml of 30 mg/L	86%--60 min	0.03 min <sup>-1</sup>	5
CuO/TiO <sub>2</sub> -GR	500 W Xe lamp	30 mg vs. 50 ml of 30 mg/L	80%--8 h	NO	6
TiO <sub>2</sub> /RGO/Ag	300 W Xe lamp	10 mg/L Conc	93% --120 min	0.017 min <sup>-1</sup>	7
RGO-CNDs	300 W Hg lamp	10 mg vs. 50 ml of 12 mg/L	90%--60 min	NO	8

## References

- [1] N. N. Shao, S. Q. Tang, Z. Liu, L. Li, F. Yan, F. Liu, S. Li, Z. T. Zhan, Hierarchically structured calcium silicate hydrate based nanocomposites derived from steel slag for highly efficient heavy metal removal from waste water, ACS Sustain. Chem. Eng. 2018. DOI: 10.1021/acssuschemeng.8b03428.

- [2] J. J. Mao, M. Z. Ge, J. Y. Huang, Y. K. Lai, C. J. Lin, K. Q. Zhang, K. Meng, Y. X. Tang, Constructing multifunctional MOF@rGO hydro-/aerogels by the self-assembly process for customized water remediation, *J. Mater. Chem. A* 5 (2017) 11873-11881.
- [3] Q. Liang, J. Jin, M. Zhang, C. Liu, S. Xu, C. Yao, Z. Li, construction of mesoporous carbon nitride/binary metal sulfide heterojunction photocatalysts for enhanced degradation of pollution under visible light, *Appl. Catal. B: Environ.* 218 (2017) 545-554.
- [4] M. Nasr, L. Soussan, R. Viter, C. Eid, R. Habchi, P. Mielead, M. Bechelany, High photodegradation and antibacterial activity of BN–Ag/TiO<sub>2</sub> composite nanofibers under visible light, *New J. Chem.* 42 (2018) 1250-1259.
- [5] X. Li, Y. Pi, Q. Xia, Z. Li, J. Xiao, TiO<sub>2</sub> encapsulated in salicylaldehyde-NH<sub>2</sub>-MIL-101 (Cr) for enhanced visible light-driven photodegradation of MB, *Appl. Catal. B: Environ.* 191 (2016) 192-201.
- [6] Y. Fang, R. J. Wang, G. H. Jiang, H. JIN, Y. Wang, X. K. Sun, S. Wang, T. Wang, CuO/TiO<sub>2</sub> nanocrystals grown on graphene as visible-light responsive photocatalytic hybrid materials, *Bull. Mater. Sci.* 35 (2012) 495–499.
- [7] H. W. Tian, C. X. Wan, X. Xue, X. Y. Hu, X. Y. Wang, Effective electron transfer pathway of the ternary TiO<sub>2</sub>/RGO/Ag nanocomposite with enhanced photocatalytic activity under visible light, *Catalysts* 7 (2017) 156.
- [8] L. Fu, X. F. Xiao, A. W. Wang, Reduced graphene oxide coupled with g-C<sub>3</sub>N<sub>4</sub> nanodots as 2D/0D nanocomposites for enhanced photocatalytic activity, *Journal of Physics and Chemistry of Solids*, 122 (2018) 104-108.